



ALICE-ANA-2017-xxx
May 17, 2017

2

3

(Anti-)Nuclei production in Pb–Pb collisions at $\sqrt{s_{\text{NN}}} = 5.02$ TeV

4

Maximiliano Puccio^{1,3}, Stefania Bufalino^{2,3}, Massimo Maserà^{1,3}

5

1. Università degli studi di Torino
2. Politecnico di Torino
3. INFN, Sezione di Torino

6

Email: maximiliano.puccio@cern.ch

7

Abstract

8

9

10

11

12

13

14

The production mechanisms of light flavoured (anti-)baryon clusters in ultrarelativistic Heavy Ion Collisions (HIC) is one of the open puzzles of the high energy nuclear physics. In this analysis note we describe the analysis method used for measuring the production spectra of (anti-)deuterons and (anti-)³He in Pb–Pb collisions at $\sqrt{s_{\text{NN}}} = 5.02$ TeV. The techniques used in this work are similar to the ones adopted for the same analyses done in ALICE for the Pb–Pb collisions data sample at $\sqrt{s_{\text{NN}}} = 2.76$ TeV. In the final section of this Analysis Note we compare the obtained spectra with those of the protons to check if the predictions of the coalescence and thermal models fit our measurements.

15 **Contents**

16	1 Nuclei and anti-nuclei in Pb–Pb collisions: analysis technique	3
17	1.1 Data and Monte Carlo samples	3
18	1.1.1 Event selection	4
19	1.1.2 Track selection	8
20	1.2 Raw spectra extraction	8
21	1.2.1 Deuteron and ^3He identification using TPC	9
22	1.2.2 Signal extraction for deuterons using TPC+TOF	11
23	1.3 Corrections to the raw spectra	13
24	1.3.1 Momentum shift correction	13
25	1.3.2 Efficiency \times Acceptance correction	14
26	1.3.3 Secondary particle background rejection	16
27	1.4 Systematic checks	18
28	2 Final results	27
29	2.1 Production spectra	27
30	2.2 Yield and mean p_{T}	30
31	2.3 Comparisons to the theoretical expectations	32
32	2.4 Nucleus over proton ratio	35
33	A Ratios anti-nuclei over nuclei	37
34	References	41

1 Nuclei and anti-nuclei in Pb–Pb collisions: analysis technique

This section describes the analysis steps required to measure the production spectra of light (anti-)nuclei in Pb–Pb collisions with the ALICE experiment. The analysis of the (anti-)deuteron production and of the (anti-) ^3He production spectra has been carried out only in Pb–Pb collision at $\sqrt{s_{NN}}=5.02$ TeV.

1.1 Data and Monte Carlo samples

The analyses presented in this thesis are based on the data sets of Pb–Pb collisions in 2015 at $\sqrt{s_{NN}}=5.02$ TeV (LHC15o period). The events were collected whenever a coincidence of signals of both sides of the V0 detector was found. Moreover, the timing information of the V0 scintillator arrays paired with the timing information from the ZDC is used as further offline rejection of events triggered by the interactions of the beams with the residual gas in the LHC vacuum pipe. After the offline event selection, the data sample consists of about 90 million Pb–Pb collisions at $\sqrt{s_{NN}}=5.02$ TeV. Figure 1 shows the distribution of the centrality percentile for the selected events. This distribution is clearly flat as a consequence of the Minimum Bias (MB) trigger strategy adopted during the 2015 Pb–Pb data taking.

The LHC15o is further divided in three subsamples according the interaction rate of the collisions and the tracking code used to reconstruct the subsamples:

- LHC15o_lowIR_pass3: corresponds to the first runs collected in the LHC15o period with low interaction rate;
- LHC15o_highIR_pass1: is the first bunch of high interaction rate runs, reconstructed with a version of the tracking code that has an issue at small p_T with the association of the correct mass hypothesis to the tracks;
- LHC15o_pidfix_pass1: is the second part of high interaction rate runs, where the issue with the wrongly associated mass hypothesis has been solved.

The list of runs used in the analysis is the intersection of the hadron PID lists recommended by the Data Preparation Group and the runs available in the MC samples with injected nuclei. The runlists

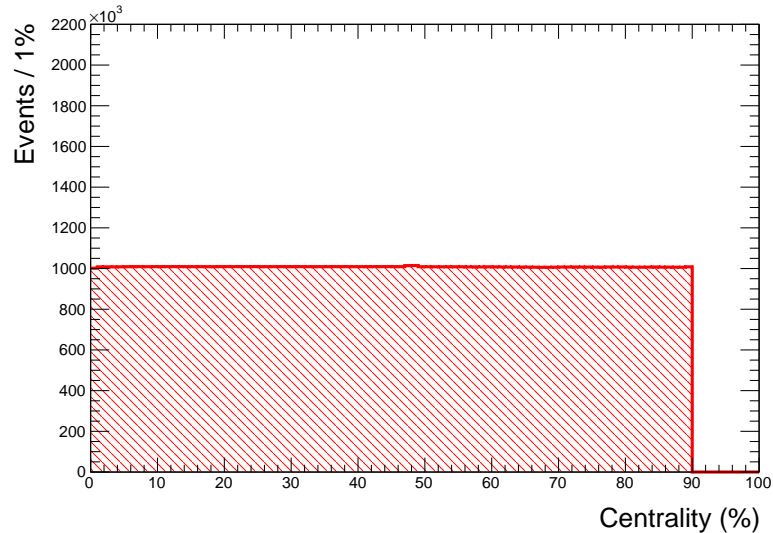


Fig. 1: V0M centrality percentile distribution in the 2015 data sample for events satisfying the event selection criteria. Increasing centrality percentile correspond to decreasing centrality of the collisions studied. The centrality estimation, as well as the definition of the V0M estimator, are discussed in details in [1].

Table 1: Details about the MC productions used in this analysis. For all of them, the particles are injected on top of an HIJING Pb–Pb event. The impact parameter (b) of the HIJING event is extracted from a flat distribution with the limits reported in the table. Each MC sample is simulated using the database of the detector conditions of the data taking period of interest, the *anchor period*. The number of injected particles reported in the third column has to be multiplied by 2 for the injection of the respective charge conjugate states.

Anchor period	b (fm)	Injected particles per event (+cc)	Events	Production name
$\sqrt{s_{\text{NN}}} = 5.02$ TeV Pb–Pb	0–5		112112	LHC16h7a
	5–11	$10 \times {}^2\text{H}, {}^3\text{H}, {}^3\text{He}, {}^4\text{He}, 40 \times {}^3_{\Lambda}\text{H}, 20 \times {}^4_{\Lambda}\text{H}, {}^4_{\Lambda}\text{He}$	439760	LHC16h7b
	11–15		355740	LHC16h7c

used for the aforementioned periods are available in the train page of the PWGLF¹ under the name of Runlist_nuclex.

The Monte Carlo (MC) samples used to compute the efficiency, acceptance and momentum shift corrections were generated using the HIJING event generator [2]. The conditions of data taking are accounted in the MC by reproducing the actual configuration of the different detectors in the runs used for the analysis. Since the HIJING event generator used to simulate Pb–Pb collisions does not provide light (anti-)nuclei, an *ad-hoc* generator that injects particles on top of a HIJING event was used. The kinematics of the injected nuclei is chosen randomly by picking their transverse momentum from a flat distribution in the range between 0 and 10 GeV/ c , their azimuthal angle from a distribution between 0 and 2π radians, and their rapidity from a flat distribution in the range $|y| < 1$. The MC simulation of a full Pb–Pb event, from the generation of the kinematics of the different particles and their transport in the detector volumes, is expensive in terms of computing resources (approximately one hour per one central Pb–Pb on the ALICE GRID). For this reason only a fraction of the total collected statistics is generated in the MC samples. The centrality of the simulated events is steered by setting the impact parameter (b) of the HIC simulated by HIJING. In the MC samples discussed here, b was picked randomly for each event. In order to optimise the use of the computing resources, three different MC samples anchored to the 2015 Pb–Pb data sample and using different b intervals were produced. These three MC productions correspond to the 0-10%, 10-50% and 50-90% V0 centrality intervals. The b intervals used as well as the details about the number of different species injected in each MC event and the number of available events are presented in Table 1. Moreover, three additional MC production (LHC16g1a, LHC16g1b and LHC16g1c) with no injected light (anti-)nuclei states are used to extract the DCA_{xy} templates for nuclei coming from secondary interactions.

1.1.1 Event selection

A further selection of the events to be analysed is performed offline to reduce possible biases from particular conditions of the data taking (e.g. high interaction rate, parts of detectors switched off). The typical selection used in Pb–Pb collision to obtain a symmetric acceptance is the rejection of events with the primary vertex outside the fiducial region of ± 10 cm in the beam direction from the nominal collision point ($|V_z| \leq 10$ cm).

Because of the high interaction rate observed in the 2015 data taking, a fraction of the triggered events contains data corresponding to more than one collision (pile-up). The first selection criterion applied to remove the pile-up is on the number of primary vertices reconstructed with SPD with more than n contributors, where n is a parameter of the selection.² From previous analyses, looking at the multiplicity

¹https://alimonitor.cern.ch/trains/train.jsp?train_id=20

²The number of contributors is the number of SPD tracklets used to estimate the vertex position. A tracklet is built by matching two hits, one in the first SPD layer and the other in the second. If a vertex is built with few tracklets, it is possibly a

Table 2: Summary of the event selection applied for the different data samples analysed in this work. See the text for the description of the used variables.

Data sample	Selections
Pb–Pb 2015 (data + MC)	$ V_z \leq 10\text{cm}$ Reject multiple SPD vertices with more than 5 contributors $ \Delta V_z \leq 20\sigma_{\text{track}}$, $ \Delta V_z \leq 10\sigma_{\text{SPD}}$ and $ \Delta V_z \leq 0.2\text{ cm}$
Pb–Pb 2015 (only data)	$ V0M - n_{\text{tracklets}} \leq 5\sigma$ $ V0M - \text{CL0} \leq 5\sigma$

dependence of the false positive pile–up tagging, the n parameter was set to 5 for events with more than 50 tracklets, to 3 for events with less than 20 tracklets and it was set to 4 for the remaining events. This method removes only the pile–up of collisions occurring either during the same bunch crossing³ or out of bunch pile–up within the SPD readout time (300 ns). The pile–up tagging method based on the SPD vertex finding is not able to resolve collisions spaced along the beam axis coordinate by less than 8 mm. In this case the pile–up is not detected and the two collisions are merged. Other selections that help reducing the effect of the pile–up background are based on the correlation of different centrality estimators. For instance, the outliers in the correlation between the centrality estimator V0M, based on the V0 detector (whose readout window is 25 ns), and CL0, based on the SPD clusters, are interpreted as events with residual pile–up. Some outliers can be spotted also in the correlation between the V0M centrality estimator and the SPD tracklets. In order to suppress such outliers, a 5σ selection has been applied on the aforementioned correlations. Figure 2a and Figure 2b show the correlation between the V0M and CL0 centrality estimators before and after the event selection⁴ respectively and it is possible to see how the applied selections clean the correlation between these variables. At the same time, the applied selections clean the correlation between tracklets and the V0M estimator (Figure 2c and Figure 2d). Another visible effect due to the very high multiplicity events, for instance those containing two piled up central collisions, is in the distribution of the z coordinate of the primary vertices. In such conditions the vertex finding algorithm using the reconstructed tracks fails to find the correct primary vertex⁵. As a consequence, the distribution of the primary vertex position along the z axis shows some spikes (Figure 3a) before the event selection and it is possible to see a large difference between the reconstructed vertex position obtained with the SPD based method and the track based vertex finding algorithm ΔV_z (Figure 3c). These discrepancies are filtered at the level of the event selection, picking only events where ΔV_z is less than $20\sigma_{\text{track}}$ and $10\sigma_{\text{SPD}}$, where σ_{track} and σ_{SPD} are the resolution of the primary vertex computed with the track based and the SPD only vertex finding algorithms respectively, and anyway is less than 0.2 cm. Figure 3b and Figure 3d show how the selection applied cure the distribution of the primary vertex position and of ΔV_z respectively. These additional selections for the pile–up rejection turn out to have a negligible effect on the final analysis results.

The above–mentioned selections are summarised in Table 2 together with the dataset to which they are applied. The main rationale behind the choice of centrality classes is the necessity of comparing the deuteron production with that of other light flavoured particles, in particular with protons. Therefore in the 2015 data sample, 10 slices in centrality have been used to perform the analysis on deuteron production: 0–5%, 5–10%, 10–20%, 20–30%, 30–40%, 40–50%, 50–60%, 60–70%, 70–80% and finally

fake.

³The bunch crossing is defined as the instant when the two LHC beams cross at the ALICE interaction point. The time windows separating two bunch crossings are always multiple of 25 ns, that is the period of the LHC clock.

⁴Here and in the following, the plots show the difference before and after the complete event selection, including the selection on the trigger scheme and all the selections reported in Table 2

⁵One possible explanation of this behaviour is that the analytical minimisation procedure used in this algorithm fails to find the global minimum in the extreme condition of pile–up of two central Pb–Pb events.

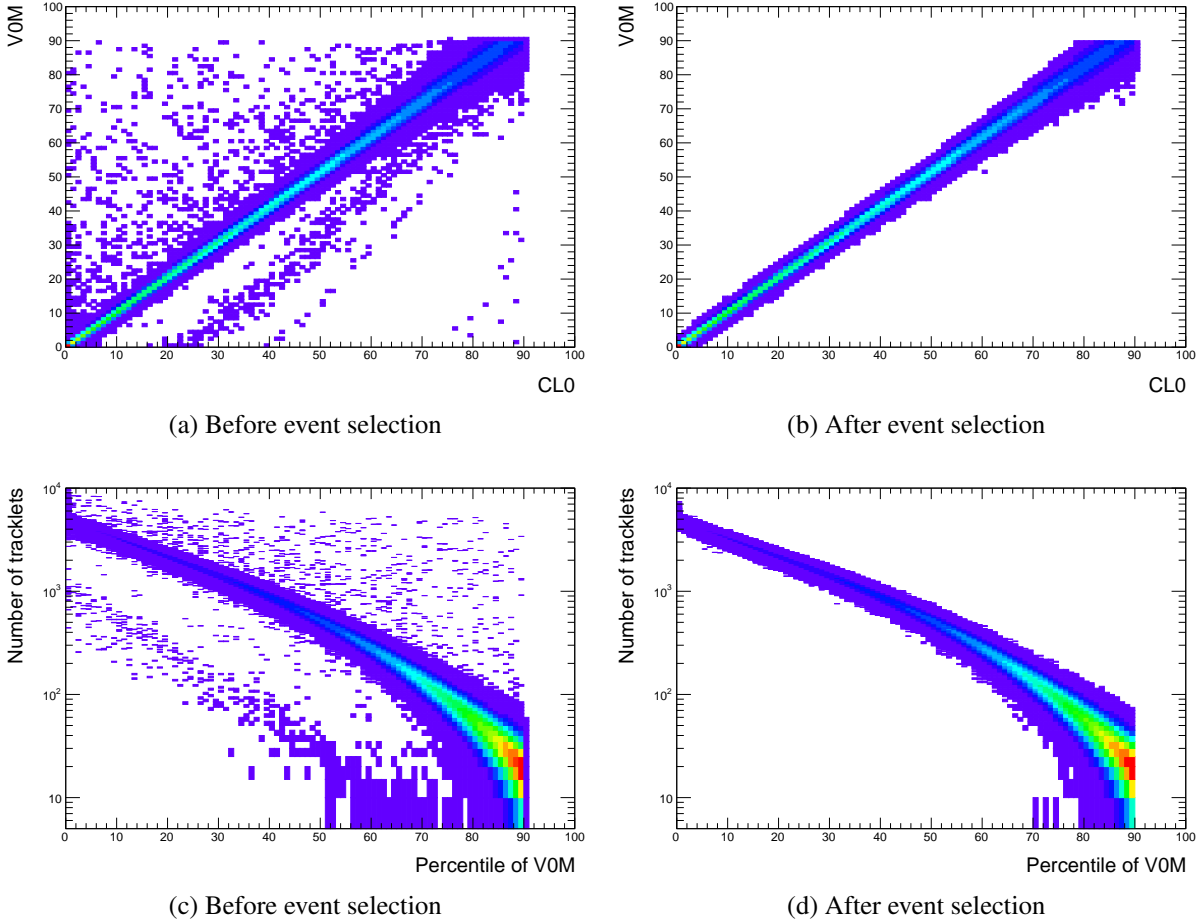


Fig. 2: Correlation plot between SPD related quantities and V0M centrality estimator. The top plots show the correlation between the CL0 centrality estimator (proxy for the number of cluster in the innermost layer of SPD) and the V0M estimator before (on the left) and after (on the right) the event selection. Similarly the bottom plots show the correlation between the number of tracklets reconstructed with the SPD and the V0M estimator.

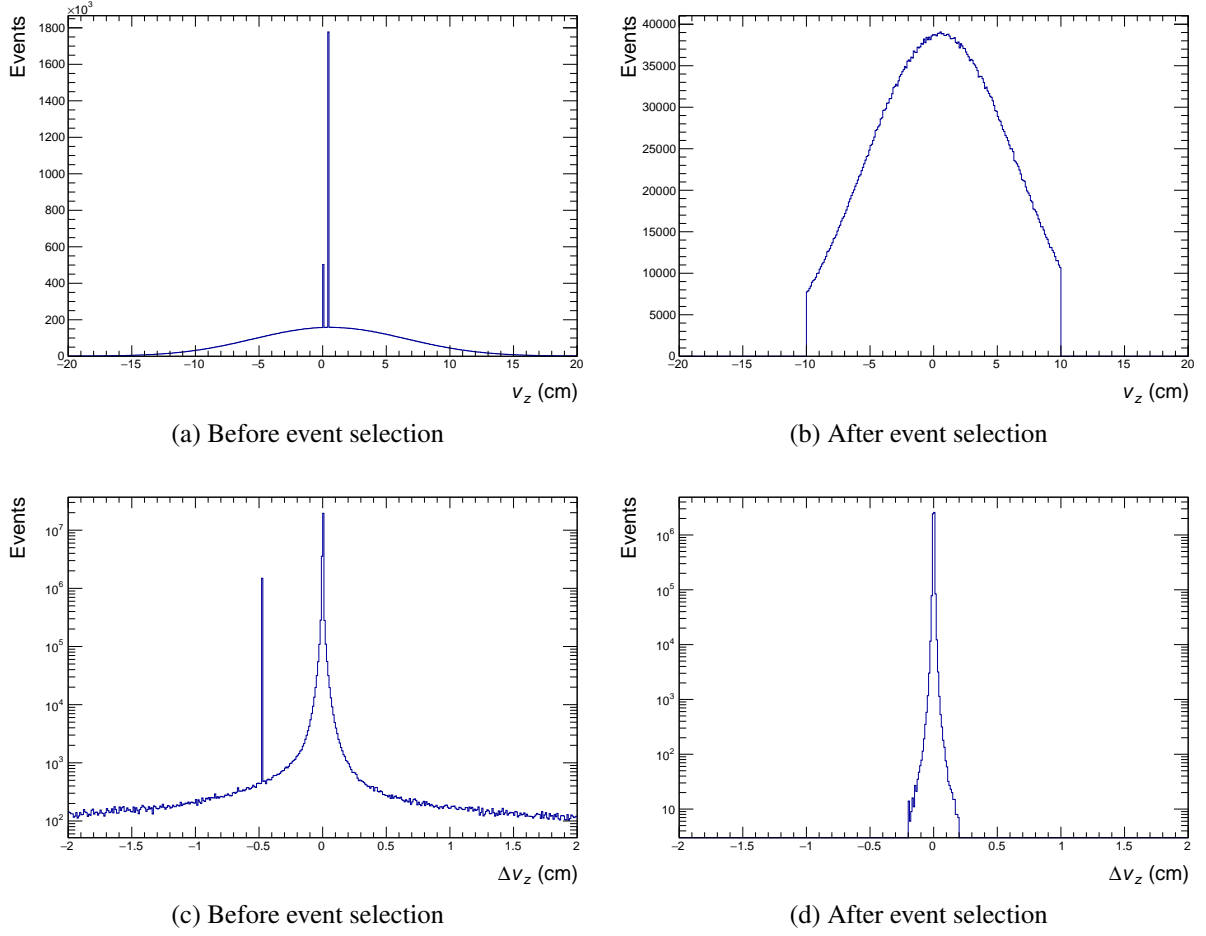


Fig. 3: Distribution of the z vertex position (top row) and of the distance between the vertex reconstructed with the track based and the SPD only vertex finding algorithms (bottom row). The left column show the distribution before the event selection while the right column show the effect of the selections on these variables.

Table 3: Summary of the track selections applied in the analyses discussed in this analysis note.

Track selections
$ \eta \leq 0.8$ and $ y \leq 0.5$
$n_{\text{TPCclusters}} > 69$, $n_{\text{ITSclusters}} > 1$ and $n_{\text{SPDclusters}} > 0$
$ \text{DCA}_z \leq 1 \text{ cm}$ and $ \text{DCA}_{xy} \leq 0.1 \text{ cm}$
$\chi^2_{\text{TPC}}/n_{\text{TPCclusters}} \leq 4$
$\chi^2_{\text{ITS}}/n_{\text{ITSclusters}} \leq 36$
Reject kink topologies

80-90%. The study of the production spectra of ^3He is more limited by the available amount of events. For this reason the analysis for the ^3He is carried out only in three centrality intervals: 0-10%, 10-40% and 40-90%. In the context of setting up the event selection for this work, I developed a general tool for applying standard event selection in ALICE analyses, AliEventCuts, that has been used to apply the above mentioned selections.

1.1.2 Track selection

The aim of the analyses presented in this thesis is to measure the primary light (anti-)nuclei production in the mid-rapidity region ($|y| < 0.5$). Primary nuclei are only those produced in the collision or in the evolution stages of the system created in a HIC. In order to use only the geometrical region in which the ALICE experiment is able to perform full tracking and to provide the best possible PID information, only tracks in the pseudorapidity region $|\eta| < 0.8$ are used in these analyses. Moreover, to guarantee a track momentum resolution of 2% in the relevant p_T range and a dE/dx resolution of about 6%, the selected tracks are required to have at least 70 clusters in the TPC and two points in the ITS (out of which at least one in the SPD). The requirement of at least one point in the SPD assures a resolution better than 300 μm [3] on the distance of closest approach to the primary vertex in the plane perpendicular (DCA_{xy}) and parallel (DCA_z) to the beam axis for the selected tracks.

In order to suppress the contribution of secondary particles only tracks with $|\text{DCA}_z| \leq 1 \text{ cm}$ are selected. The main secondary deuteron contribution comes from the knock-out deuterons produced by the interaction of primary particles with the material of the beam-pipe and of the apparatus and it is relevant for the production spectra and the elliptic flow measurements for $p_T \leq 1.4 \text{ GeV}/c$. The only known contribution to secondary deuterons and anti-deuterons from weak decays comes from the charged three-body decay of the hypertriton ($^3_\Lambda\text{H} \rightarrow \text{d} + \text{p} + \pi^-$) and of the anti-hypertriton ($^3_{\bar{\Lambda}}\bar{\text{H}} \rightarrow \bar{\text{d}} + \bar{\text{p}} + \pi^+$). From the measurement of the hypertriton production into charged two-body decay [4] we know that this contribution is negligible. Moreover, the χ^2 per TPC cluster is required to be less than 4 and the χ^2 per ITS cluster is required to be less than 36. Finally tracks of weak-decay products are rejected as the deuteron is a stable nucleus. When the TOF PID is required, a hit matched to the track extrapolation in the TOF sensitive area is required.

The aforementioned track selection criteria are common to the (anti-)deuteron and (anti-) ^3He and Table 3 summarises them.

1.2 Raw spectra extraction

The identification of (anti-)deuteron and (anti-) ^3He is performed in the analyses reported here using a combination of the particle identification tools provided by the TPC and the TOF for the deuteron, and using the TPC information alone for the (anti-) ^3He .

In the following subsections the details about the identification and signal extraction for the light nuclei will be presented.

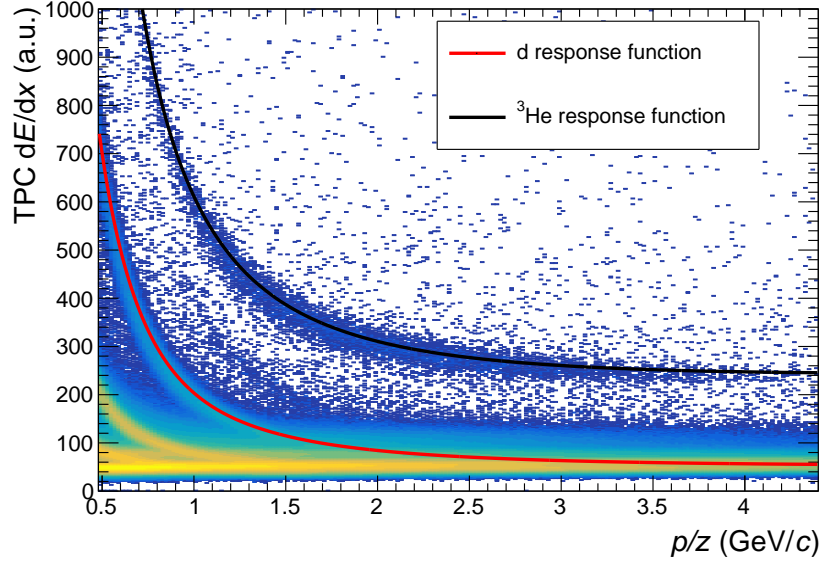


Fig. 4: Specific energy loss in the TPC active volume for negative particles as a function of the particle rigidity in Pb–Pb collisions at $\sqrt{s_{NN}}=5.02$ TeV. The solid lines represent the expected TPC response for deuterons (red) and ^3He (black).

1.2.1 Deuteron and ^3He identification using TPC

The specific energy loss of particles inside the active volume of the TPC can be used to determine their identity.

Figure 4 show the specific energy loss for negative particles in the TPC active volume and the expected signal for deuterons and ^3He for the 2015 Pb–Pb data sample.

Since the deuteron is twice as massive than the proton, it reaches the minimum of ionisation at $p \sim 1.8$ GeV/c. Due to the finite resolution on the specific energy loss measured by the TPC ($\approx 6\%$ for the selected tracks) and due to the contamination from electrons and positrons, a track-by-track identification of deuterons can be performed using exclusively a fiducial selection on the TPC dE/dx information only up to $p \sim 1$ GeV/c. At higher momenta the identification of deuterons becomes less trivial and the statistical unfolding of the deuteron signal from the minimum ionising particles signal and the electron/positron contamination has to be performed. For sake of simplicity, in this work the identification of the deuteron is achieved by using the combined TPC and TOF information.

Conversely, for the ^3He , that has charge $z = 2e$, the sole TPC information provide a clean identification. This can be evicted remembering that the Bethe–Bloch formula for the specific energy loss depends on the square of z , thus the ^3He is well separated by all the particle species with $z = 1e$ in a large momentum region.⁶ The only known species that might contaminate the identification of the ^3He in the TPC is the ^4He , but since its expected production rate is approximately 300 times smaller than the expected production of ^3He , it can be neglected in this analysis. In the low momentum region, the specific energy loss of ^3He becomes similar to the one of the ^3H and therefore this contamination has to be subtracted in the signal extraction.

⁶On top on the z^2 dependence, the Bethe–Bloch formula depends also on the particle Lorentz factors, β and γ :

$$\left\langle \frac{dE}{dx} \right\rangle \propto \frac{z^2}{\beta^2} \log \left(\frac{2\gamma^2 \beta^2 m_e}{I_0} \right). \quad (1)$$

In the formula m_e is the electron mass and I_0 is the minimum energy loss

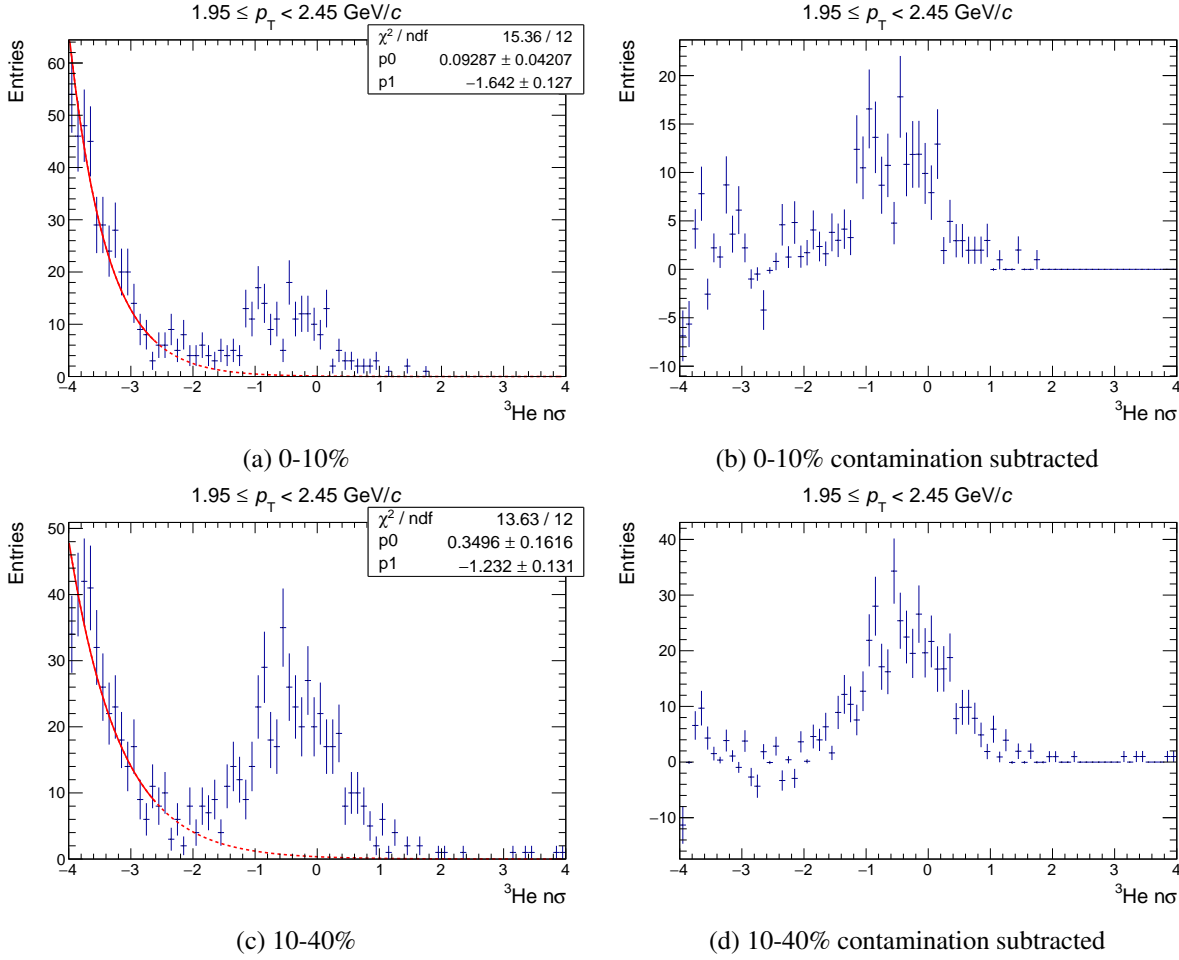


Fig. 5: $n\sigma$ distributions for ${}^3\text{He}$ in the $1.95 \leq p_T < 2.45 \text{ GeV}/c$ bin before (on the left) and after (on the right) the subtraction of the contamination from ${}^3\text{H}$. The red lines show the fitted function, represented as a solid line in the fit range.

In order to extract the number of produced ${}^3\text{He}$ in a particular transverse momentum interval, the number of entries in the $n\sigma$ distribution is counted. The $n\sigma$ distributions are filled with the difference between the specific energy loss associated to all the selected tracks and the expected (anti-) ${}^3\text{He}$ dE/dx , normalised on the TPC dE/dx resolution on the specific energy loss σ . The signal of the ${}^3\text{He}$ is expected around 0σ but as it is shown in Figure 4 the parametrisation of the expected response for ${}^3\text{He}$ is not perfectly centred around zero even if the trend is rather well reproduced. The maximum shift observed is of 0.5σ on the negative side. For the purpose of the spectra analysis the centring of the $n\sigma$ distributions is not fundamental, as the entries can be computed starting from the mean of the observed distribution within a 3σ interval. Figure 5a and Figure 5c show an example of the $n\sigma$ distribution for ${}^3\text{He}$ for the 0-10% and 10-40% centrality ranges respectively: these particular distributions correspond to a p_T interval between 1.95 and $2.45 \text{ GeV}/c$. In this p_T interval the contamination from the ${}^3\text{H}$ is visible on the left of the peak of the ${}^3\text{He}$ distribution. A fit with an exponential function is performed on the tail of the ${}^3\text{H}$ contamination, where no ${}^3\text{He}$ signal is expected. The resulting exponential function is then subtracted to the data histogram to obtain the distribution of the ${}^3\text{He}$ candidates without any significant residual background (Figure 5b and Figure 5d). This contamination from ${}^3\text{H}$ is present only when analysing at the production of ${}^3\text{He}$ and it is due to secondary ${}^3\text{H}$ nuclei from knock-out interactions of other primary particles with the experiment material. For this reason, such a contamination it is not present in the $n\sigma$ distributions for the ${}^3\text{He}$. Finally, Figure 6a and Figure 6b show the raw counts extracted with the

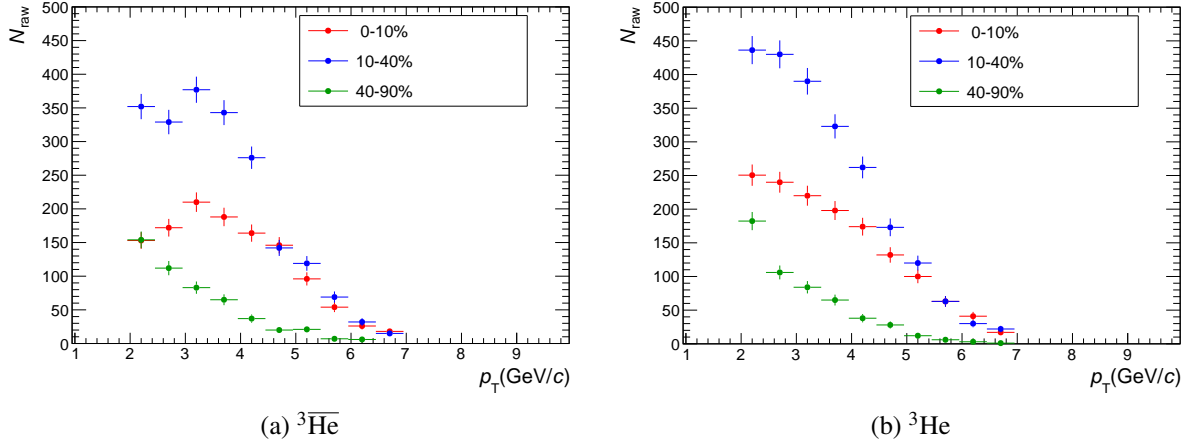


Fig. 6: Raw counts for ${}^3\text{He}$ and ${}^3\overline{\text{He}}$ in the p_T range where the procedure for the signal extraction described in the text was feasible.

procedure mentioned above.

1.2.2 Signal extraction for deuterons using TPC+TOF

The signal extraction for (anti-)deuterons is performed combining the information of the specific energy loss measured by the TPC with that of the time of flight measured by the TOF. For this reason an additional track requirement is set for the deuteron analysis: a hit matched in the TOF detector that provides, as its name suggests, an accurate measurement of the time of flight t_{TOF} of a particle. The Lorentz β of the particle can be measured using in addition the track length L measured in the tracking procedure:

$$\beta = \frac{L}{t_{\text{TOF}} c}, \quad (2)$$

where c is the speed of light. Combining this piece of information with the measured particle momentum p , the particle mass can be estimated as:

$$m = \frac{\sqrt{1 - \beta^2}}{\beta} p. \quad (3)$$

(Anti-)deuterons can be separated from lighter species over a wide momentum range thanks to the excellent TOF timing resolution (≈ 80 ps in Pb–Pb collisions). Nevertheless, a clean identification without background it is not possible in Pb–Pb events because of the background from mismatched TOF hits: in high multiplicity events the TOF occupancy is such that, within the track extrapolation resolution in the TOF active volume, it is possible to match more than one hit. When more than one hit can be associated, the closest to the track extrapolation is chosen. Nevertheless, the probability of associating a hit corresponding to another particle is not negligible ($\sim 20\%$ for pions at 1 GeV/ c in the most central Pb–Pb collisions [5]) and it is higher for low momentum particles. The presence of mismatched hits can be seen in the PID plots as hits not corresponding to any particle species expected signal. In this analysis to remove effectively this background a 3σ track selection criterion around the expected energy loss of (anti-)deuterons in the TPC volume is used. This selection criterion helps to reduce the background from mismatched TOF hits in the p_T region where the TPC provides a good separation of deuteron from the lighter species (up to $p_T \sim 1.8$ GeV/ c).

Figure 7 shows two examples each, one at low p_T and the other at higher p_T , of the distribution of the measured mass squared m^2 shifted by the squared nominal mass of the (anti-)deuteron m_{PDG}^2 . The distributions (Figure 7a and Figure 7b) show a deviation of m^2 at low p_T from the nominal mass of the

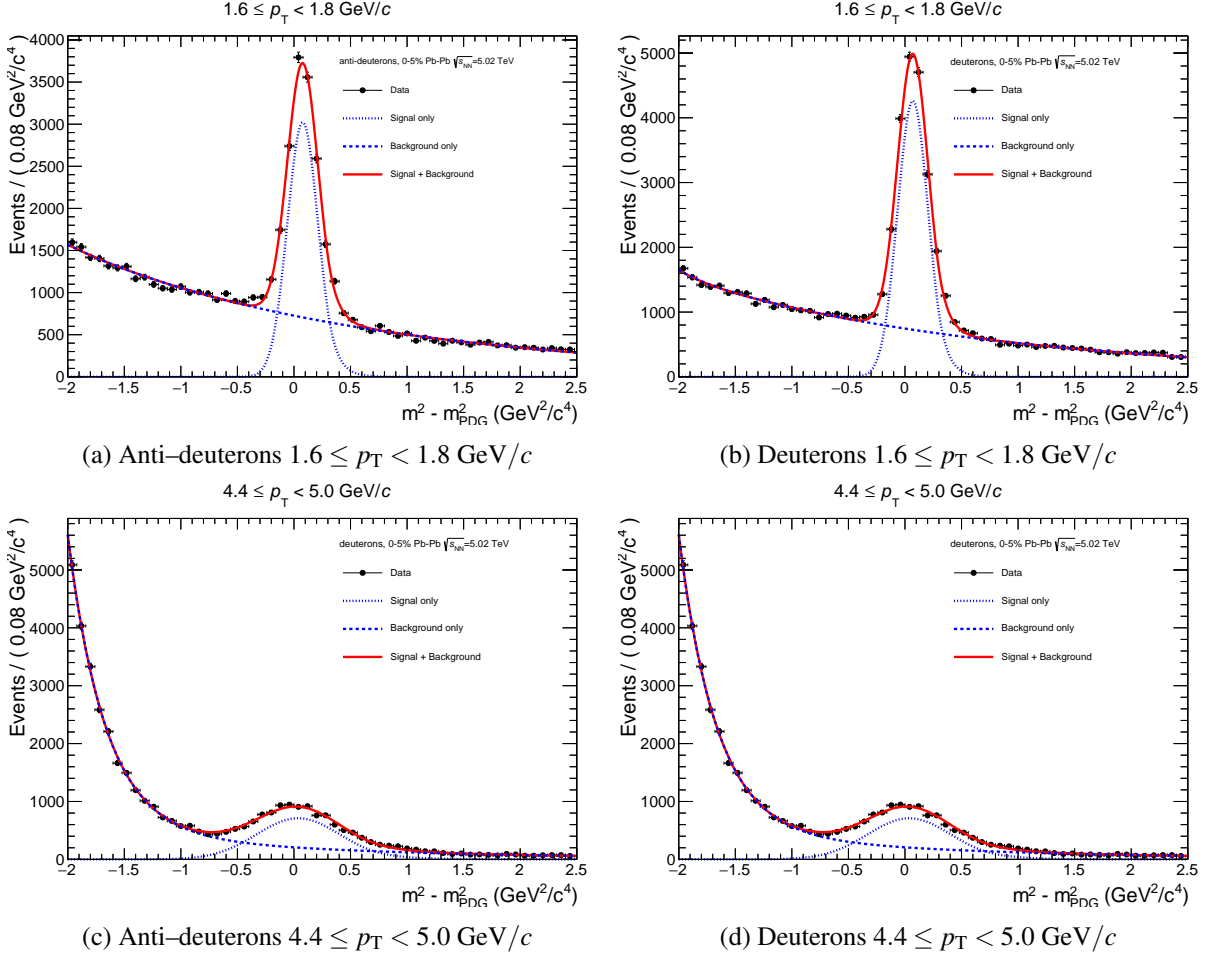


Fig. 7: $m^2 - m_{\text{PDG}}^2$ distributions for anti-deuterons (left) and deuterons (right) in two p_T bins (top and bottom) extracted in the 0-5% centrality interval of the 2015 dataset. The dashed line and the dotted line are the background and signal components of the model respectively. The red line represents the total fit to the distributions.

(anti-)deuteron that was not present in the Pb-Pb at $\sqrt{s_{\text{NN}}} = 2.76$ TeV sample. This difference could be symptom of some issues in the measurement of masses corresponding to long times of flight (i.e. small β). Such a discrepancy is anyway not affecting the signal extraction for the (anti-)deuterons. Indeed the signal extraction is performed using a two component fit to the mass spectra in order to unfold the background component from the (anti-)deuteron signal. The (anti-)deuteron signal S is modelled using a Gaussian distribution with an exponential tail:

$$S(x; N_{\text{raw}}, \mu, \sigma, n) \propto N_{\text{raw}} \begin{cases} \exp \left[-\frac{1}{2} \left(\frac{x-\mu}{\sigma} \right)^2 \right] & \text{for } x \leq \mu + n\sigma \\ \exp \left[-n \left(\frac{x-\mu}{\sigma} - \frac{n}{2} \right) \right] & \text{for } x > \mu + n\sigma \end{cases} \quad (4)$$

where N_{raw} is the number of signal counts, μ and σ are the mean and the standard deviation of the gaussian respectively, while n is the number of σ s at which S becomes an exponential function⁷. All these parameters are free to vary in the fitting procedure, thus the shift in the $m^2 - m_{\text{PDG}}^2$ distribution can be easily recovered by the determination of the μ parameter in the fit. The slope of the exponential is defined such that the S function and all its derivatives are continuous and differentiable. The function used for modelling the background is the sum of two exponentials: one exponential is used to model

⁷My code implementing this function, as well as its proper normalisation are reported in [6].

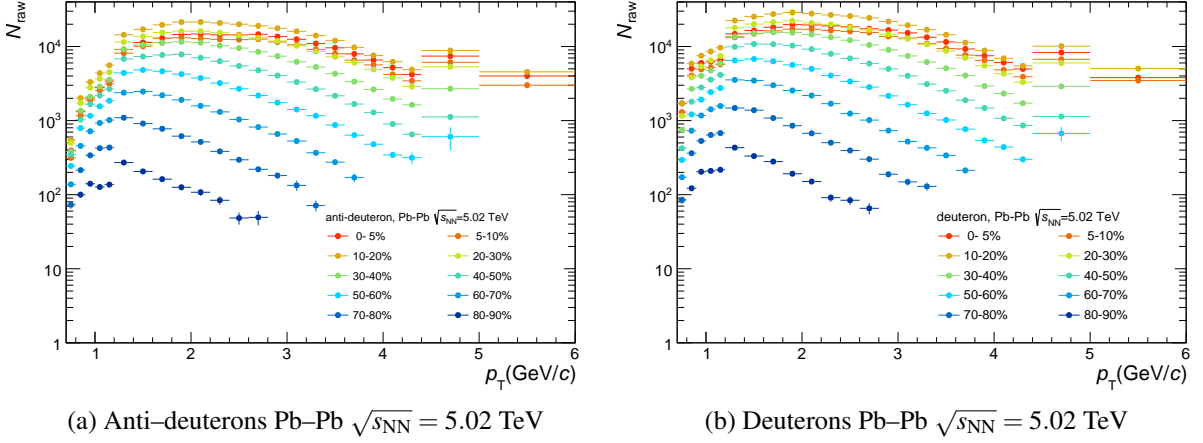


Fig. 8: Raw yields for anti-deuterons (left) and deuterons (right) represented with different colours for the different centrality classes.

the background from mismatched TOF hits shape around the signal peak while the second one is used to model the tail of the proton distribution at high p_T (e.g. Figure 7c). Since N_{raw} is one of the fit parameters its uncertainty is directly taken by the output of the fitting procedure. Figure 8 show the raw yield spectra for deuterons and anti-deuterons in the different centrality classes. Only the range in which the signal extraction could be performed is shown. The main factor that limits the p_T region of the raw yield extraction is the available amount of events and the stability of the corrections applied to the raw spectra.

1.3 Corrections to the raw spectra

The raw yields extracted in the previous section must be corrected to obtain the real production spectra. There are four major effects to be corrected for the nuclei production spectra: the tracking efficiency, the detector acceptance, the momentum reconstruction imperfections and the contamination from secondary particles. In this section the strategies adopted to correct for these effects are described.

1.3.1 Momentum shift correction

During the track fitting step of the track reconstruction algorithm, the mass hypothesis of the tracked particle is used to properly keep into account the energy loss of the particle when it traverses the detector material. This mass hypothesis is computed after a first fitting pass, using the information about the energy loss of the particle in the TPC and a first rough estimation of the momentum of the particle. A mass hypothesis for nuclei was not available in the tracking algorithm when the Run 1 samples were reconstructed, thus they were reconstructed using the mass hypothesis of the pion. The assumption of such a lighter or heavier mass biases the momentum estimation at low p_T , where the difference between the energy loss of a pion and the one of a nucleus matters mostly.

Since from the beginning of the Run 2 of the LHC, the track reconstruction has been changed to use also the nuclei mass hypothesis in the track fitting when relevant. This can be easily spotted in a similar study carried out on the 2015 data samples for both (anti-)deuterons and (anti-) ^3He (Figure 9). The reconstructed p_T for the (anti-)deuterons reproduces accurately the true momentum of the generated particle, with a mean deviation of less than 2 MeV/c.

On the other hand, the true (anti-) ^3He momentum is not reconstructed accurately for $p_T \leq 2$ GeV/c, where a deviation can be spotted (Figure 9b). This time the observed deviation points to an overestimation of the reconstructed momentum, due to the use of the ^4He mass hypothesis in the track fitting.

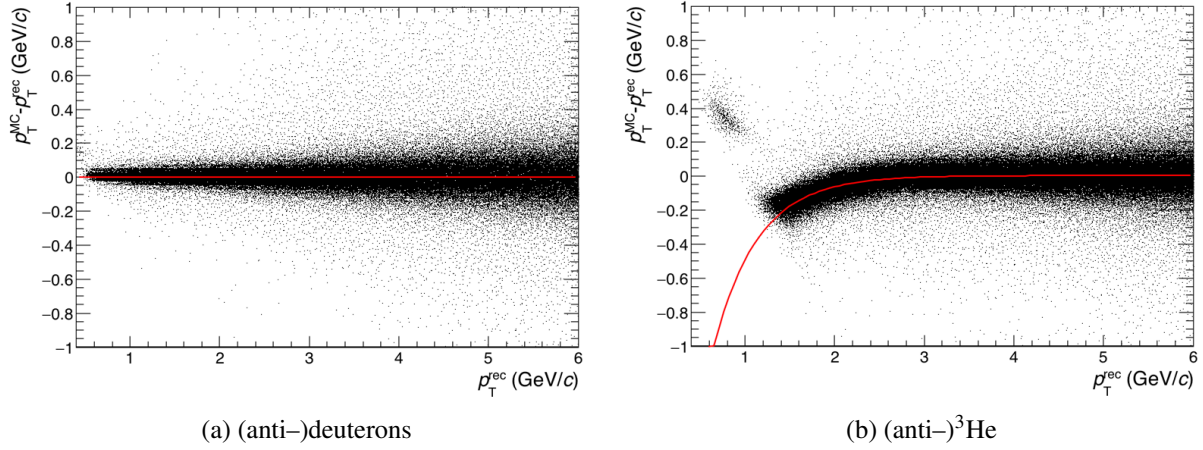


Fig. 9: Difference between the true p_T of (anti-)light nuclei (deuterons on the left, ^3He on the right) and the reconstructed one as a function of the reconstructed momentum in the 2015 dataset. The red line represent a fit to this distribution used to correct the measured momentum at the analysis level track-by-track.

The mass hypothesis is chosen among the particles whose expected dE/dx is compatible with the one observed with the track. For ^3He and ^4He this specific energy loss is very close for $p_T \leq 2 \text{ GeV}/c$. This, summed with the fact that the expected response available in the central framework of ALICE are not perfectly tuned for light-nuclei and that the mass hypothesis is chosen at a stage where only rough estimates of the track parameters and dE/dx in the TPC are available, makes the ^4He the default choice for ^3He in that p_T region. To recover the correct momentum, a fit to that distribution has been performed using the *ad-hoc* function

$$f(p_T^{\text{rec}}) = a + \exp(bp_T^{\text{rec}} + c), \quad (5)$$

and the resulting parametrisation has been used to correct track-by-track the reconstructed momentum of the (anti-) ^3He candidates. Nevertheless, the true momentum for the (anti-) ^3He is reconstructed correctly in the region of interest of the analysis presented here ($p_T > 2 \text{ GeV}/c$).

1.3.2 Efficiency \times Acceptance correction

Tracking algorithms, even if optimised, are not fully efficient in the reconstruction of particle trajectories. Even if they would be fully efficient, other inefficiency sources would affect the reconstruction. For instance, the active area of the experiment is not hermetic by design (e.g. the sector edges of the TPC) and, sometimes, parts of the detectors might be switched off because of data taking constraints (e.g. some modules excluded from the data acquisition in the SDD because they lack of stability during the data taking).

It is possible to correct for the finite efficiency and acceptance using a MC simulation where the full geometry and data taking conditions are reproduced. The number of particles crossing the detector is known when using a MC simulation and the efficiency can be defined as:

$$\text{Efficiency} \times \text{Acceptance}(p_T^{\text{rec}}) = \frac{N_{\text{rec}}(p_T^{\text{rec}})}{N_{\text{gen}}(p_T^{\text{gen}})}, \quad (6)$$

where p_T^{gen} and p_T^{rec} are the p_T generated by the event generator and the p_T measured by the tracking algorithm respectively; N_{gen} is the number of particles generated in the azimuthal region $0 \leq \phi < 2\pi$ and in the rapidity region $|y| < 0.5$. N_{rec} is the number of tracks corresponding to one of the particle species of interest satisfying the selection criteria summarised in Table 3. On top of those criteria, a hit matched

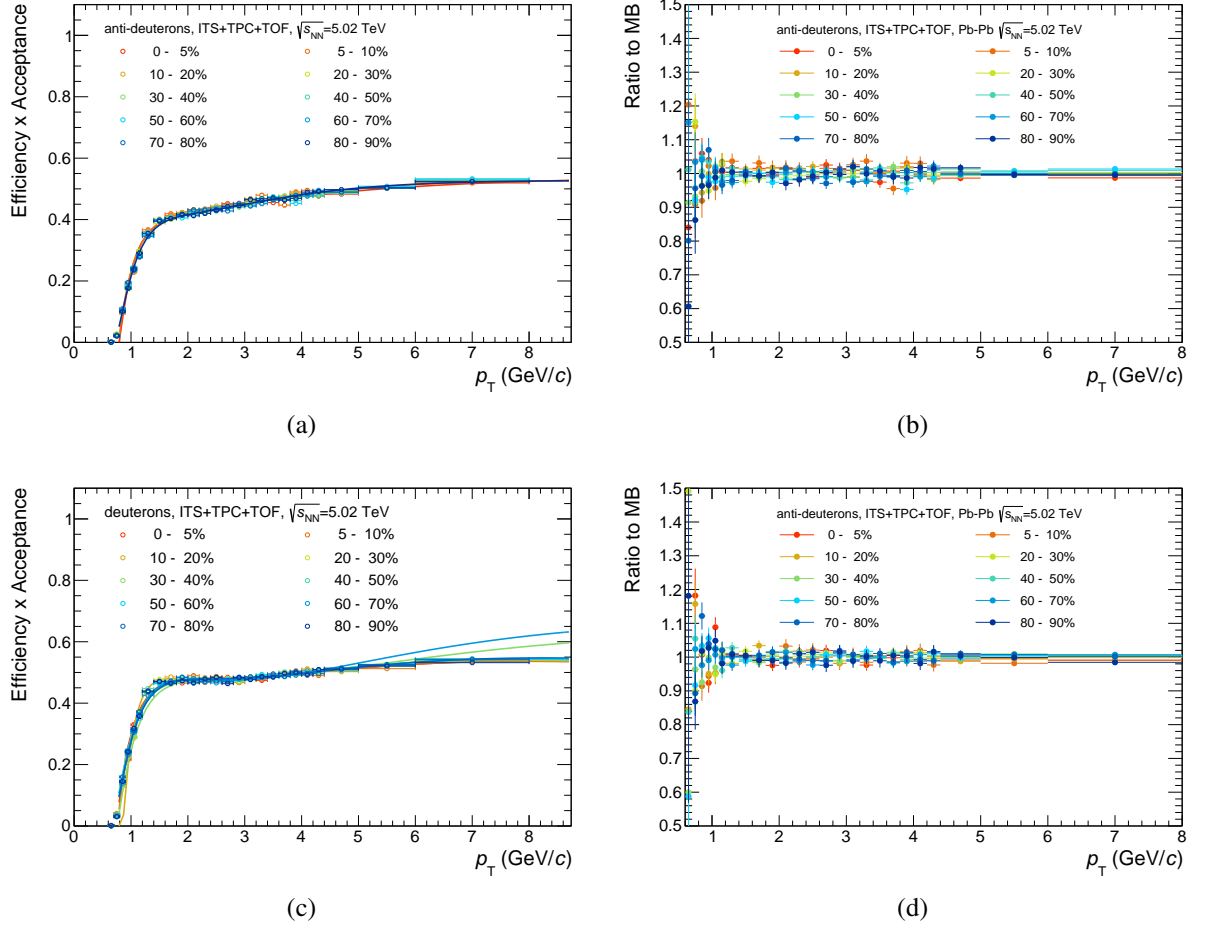


Fig. 10: On the left: anti–deuteron (top) and deuteron (bottom) efficiency times acceptance computed as a function of the centrality for the 2015 datasets. On the right: ratio between the efficiency times acceptance computed in centrality bins and the one computed without any centrality selection for (anti–)deuterons (top) and deuterons (bottom).

in the TOF detector is required for (anti–)deuterons, since the identification strategy for them is based on the TOF PID capabilities. The reconstructed p_T and the generated one are used at numerator and denominator respectively to keep into account the possible shift between p_T intervals due to the residual mismatch between the reconstructed momentum and the generated one (see the previous subsection).

No centrality dependence is visible for (anti–)deuterons in the Pb–Pb at $\sqrt{s_{NN}}=5.02$ TeV sample. Already from the plot of the efficiency \times acceptance as a function of the p_T in the centrality classes used for the analysis (Figure 10a and Figure 10c) it is possible to see that the curves corresponding to different centrality bins are not distinguishable. This can be also observe quantitatively by computing at the ratios between the centrality dependent corrections and the Minimum Bias (MB, i.e. without any centrality selection) correction (Figure 10b and Figure 10d). From these ratios it is possible to conclude that there is no clear trend with centrality of the acceptance \times efficiency for (anti–)deuterons. For this reason the MB efficiency \times acceptance is used to correct the raw spectra in all the centrality classes in order to profit from better statistical uncertainties in the determination of the correction. This is not possible for (anti–) ^3He , since the acceptance \times efficiency for these particles shows a trend with centrality (Figure 11 and its subfigures).

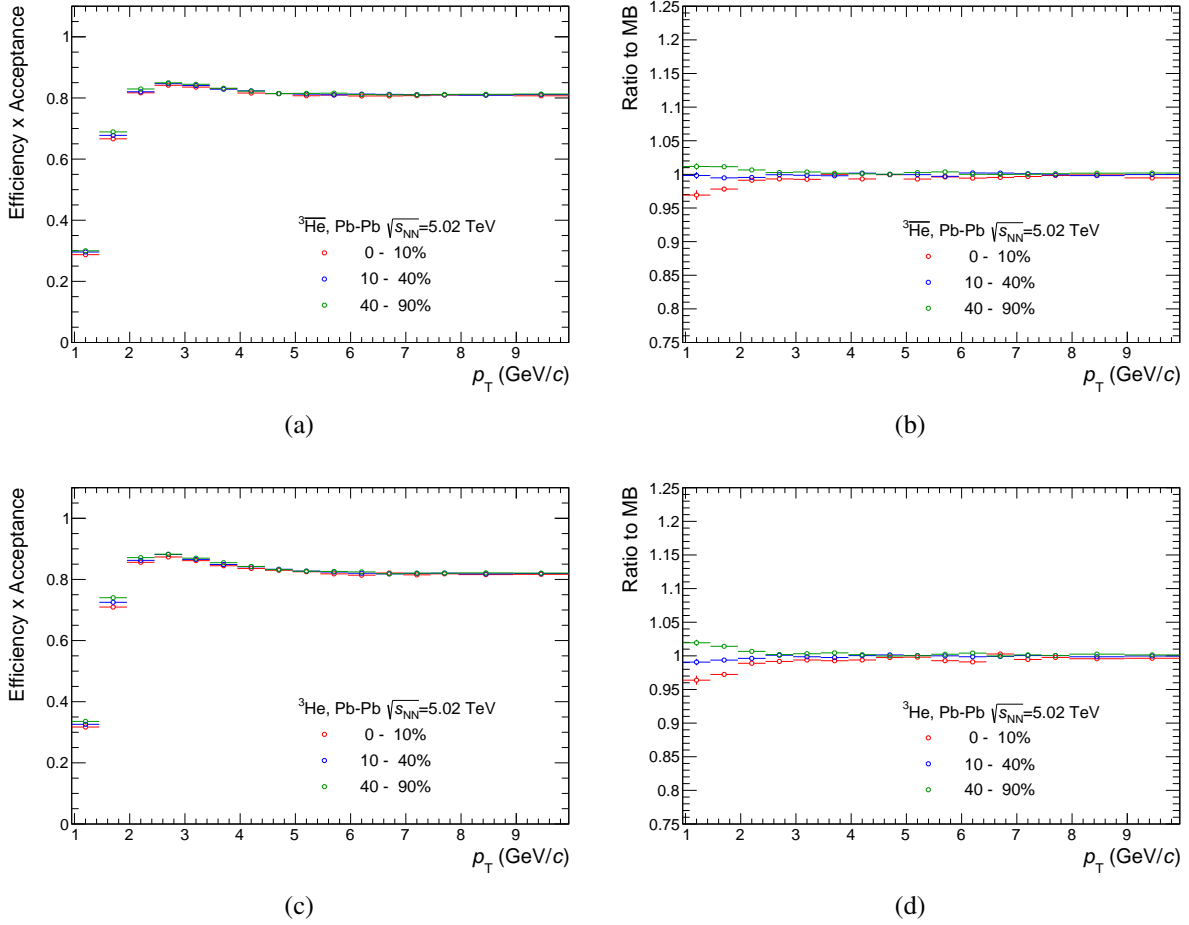


Fig. 11: On the left: anti-³He (top) and ³He (bottom) efficiency times acceptance computed as a function of the centrality for the 2015 datasets. On the right: ratio between the efficiency times acceptance computed in centrality bins and the one computed without any centrality selection for (anti-)³He (top) and ³He (bottom).

303 The acceptance \times efficiency correction is fitted with an ad-hoc function

$$f(p_T) = a_0 + a_1 e^{a_2 p_T} + a_3/p_T + a_4/(p_T)^2, \quad (7)$$

304 to check if some statistical fluctuations in the efficiency \times acceptance correction could affect the final
 305 result. The raw spectra are then corrected using both the fit function and the binned correction to evaluate
 306 possible differences in the two approaches: the difference between the two cases is found to be less than
 307 1%, and thus negligible, in the p_T range of interest of the analyses here presented.

308 1.3.3 Secondary particle background rejection

309 One of the main source of background in the analysis of the nuclei production spectra is the detection
 310 and reconstruction of nuclei coming from secondary interactions. These secondary nuclei come mostly
 311 from the interactions of other primary particles with the detector material. In some of these interactions, a
 312 light nucleus can be produced by means of knock-out processes. The typical momentum of, for instance,
 313 deuterons produced with such processes is less than 1.4 GeV/c. While for the deuteron production
 314 spectra it is important to correct for the knock-out production, the p_T region in which the ³He productions
 315 is studied is unaffected by this source of background. The baryon number conservation sets a very high
 316 energy threshold for the production of secondary anti-nuclei with similar processes, thus in the following

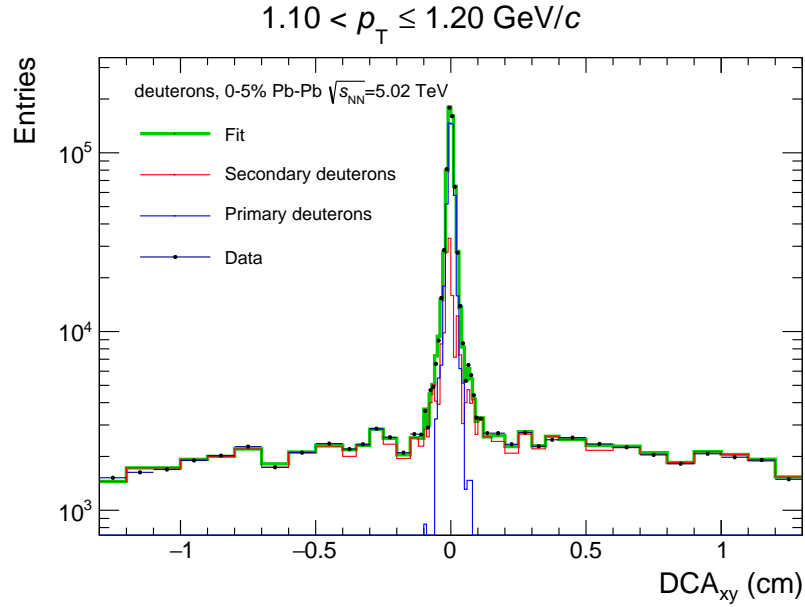


Fig. 12: Fit to the DCA_{xy} distribution (black points) of deuteron candidates. The green line is the fit result and it represents the sum of the primary particle component (blue line) and secondary particle one (red line).

only the case of nuclei will be discussed. Other processes, such as the decay of (anti-)hypernuclei, represent a negligible fraction of the observed (anti-)deuterons. On the contrary, the decay of (anti-)hypernuclei represents a significant systematic uncertainty for the (anti-) ^3He production as no effective correction can be put in place in this case, as it will be discussed in the next Section.

To remove the contamination from secondary deuterons it is possible to study the Distance-Of-Closest approach distributions on the transverse plane (DCA_{xy}) of the deuteron candidates. Primary particles are expected to have a distribution with a clear peak at $DCA_{xy} = 0$ cm, that is the expected value for particles coming from the primary vertex. On the other hand, secondary particles are expected to have a flat DCA_{xy} distribution at the first order. Unfortunately this is not the case: sometimes⁸ the tracks corresponding to secondary particles are associated to a wrong cluster in the SPD. If this SPD cluster belongs to a primary particle, the extrapolation of the track corresponding to the secondary particle will anyway point to the primary vertex, as the track pointing is given mostly by the SPD clusters. For this reason, a fit to the observed DCA_{xy} distribution is done to extract the primary fraction of observed deuterons using histogram templates for the primary particles and secondary particles component. The histogram templates used for the fit are filled from MC production, where both the identity and the origin of every particle are known. An example of a fit to the DCA_{xy} distribution is shown in Figure 12, where it is possible to see that the secondary particle component has, as anticipated, a peak structure at $DCA_{xy} = 0$ cm. The fit is done in a range of DCA_{xy} wider than the actual track selection criterium to better constrain the fit of the secondary particles component, that populates mostly the tails of the DCA_{xy} distribution. Then to obtain the fraction of primary deuterons in the region allowed by the track selection criterium, the fitted primary particles component and the total fit are integrated in that region and the primary fraction is computed from those integral. The fit has been done using the algorithm implemented in the ROOT TFractionFitter class [7]. This algorithm enables the possibility of fitting of an experimental distribution using MC generated samples, keeping into account the statistical uncertainties on the MC histograms in the likelihood maximisation. This is attained by considering the true value of each bin of the MC samples as one fit parameter. As a result, the MC components fitted to the data will not have exactly the same

⁸in less than the 10% of the cases in the most central Pb–Pb collisions

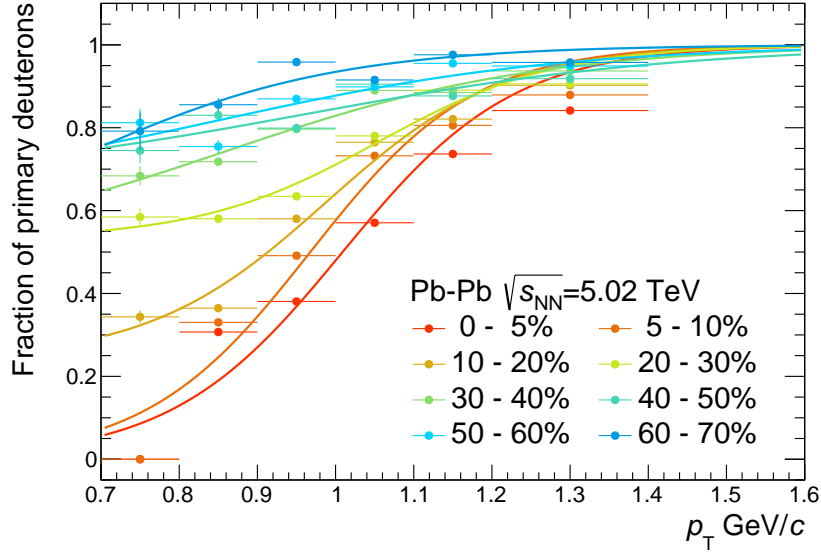


Fig. 13: Primary fraction of selected deuterons as a function of the transverse momentum. The different colours correspond to different centrality classes. The solid lines represent the fits to the distributions.

shape they had before being fed to the fitting algorithm.⁹

The fraction of primary particles as a function of the transverse momentum, has been computed in all the centrality bins covered by this analysis and it is shown in Figure 13. From this Figure it is possible to see a clear dependence of the fraction of primary deuterons with centrality: in peripheral events (i.e. low multiplicity events) the fraction of primary deuterons is higher than in central events (i.e. high multiplicity events). This can be easily understood as the higher is the flux of particles in the detector material, the higher is fraction of secondary particles observed in the detector. Since the obtained distribution of primary fraction shows some statistical fluctuations, the final correction $f_p(p_T)$ is obtained by fitting the distribution with the function:

$$f(p_T) = a + \frac{1-a}{1+be^{cp_T}}, \quad (8)$$

with $0 \leq a < 1$, $b > 0$ and $c < 0$. The resulting fits are shown as solid lines in Figure 13. A large MC sample has been used to create the template histograms for the secondary particles but it was not sufficient to have stable templates in the most peripheral events (from 70% to 90% of centrality). Nevertheless, the corrections in those bins are expected to be small and the systematic contribution of secondary particles to these centrality classes is evaluated by varying the DCA_z track selection, that is particularly sensitive to the presence of secondary deuterons, as it will be shown in the next Section.

1.4 Systematic checks

A set of systematic checks is performed to evaluate if and how much the results presented in this work are affected by systematic uncertainties. The checks performed in this context can be classified in three groups:

1. checks on the efficiency×acceptance correction, done by varying the material budget used in the

⁹For this reason this method is potentially dangerous: if the statistical uncertainties of the MC samples are big, the likelihood maximisation can almost adapt any input shape to the data. In general this method is safe only if the user checks carefully that the input MC shapes are well defined and not affected by large statistical fluctuations. The statistical uncertainty of the MC templates used in this analysis were properly checked and were suitable for the use of the TFractionFitter.

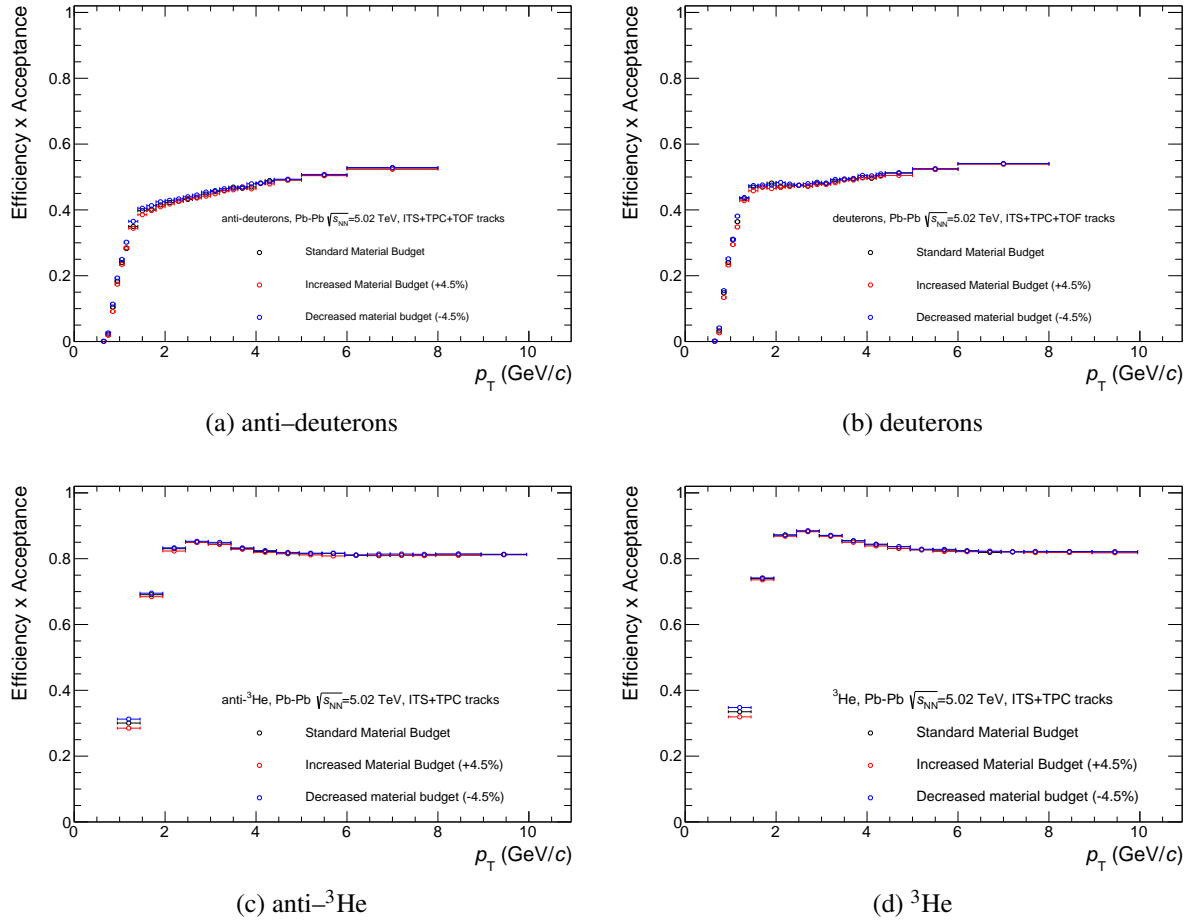


Fig. 14: Study of the effect of the material budget variation on the acceptance \times efficiency for (anti-)deuterons (top) and (anti-) ^3He (bottom).

- 363 MC simulation of the ALICE apparatus and by changing the transport code used to simulate the
 364 passage of particles through the detector material;
- 365 2. checks on the track selection criteria, carried out by varying the selection parameters and studying
 366 how they affect the final results;
- 367 3. finally the checks on the raw yield extraction.

368 When one of these checks finds a discrepancy in the obtained results, this discrepancy is kept into account
 369 to quantify the systematic uncertainty.

370 The systematic uncertainty quoted for each of the aforementioned checks is estimated as the standard
 371 deviation of the distribution of each possible systematic uncertainty source.

372 The checks on the efficiency corrections required the simulation of additional MC samples to inquire
 373 into possible discrepancies in the evaluated reconstruction efficiency when changing the material budget
 374 estimation of the experimental apparatus. The material budget variation has been chosen taking into
 375 account the uncertainty on its determination. This last point has been driven by the results obtained from
 376 the photon conversion analyses performed in ALICE¹⁰. Two additional MC samples were then produced,
 377 one with the material budget increased by 4.5% and one with the material budget decreased by the same

¹⁰ALICE collaboration work in progress.

amount. The efficiency \times acceptance evaluated in this way are shown in Figure 14 for the 2015 data sample. It is possible to see at a first glance a clear trend with the material budget in each p_T interval, with a more pronounced difference in the efficiency \times acceptance estimation at low p_T , as it was expected since low momentum particles lose more energy in the traversed material and the efficiency is rapidly changing in there. For each momentum bin analysed, the variations of the efficiency \times acceptance induced by the change of the material budget in the simulation are supposed to follow a uniform distribution around the efficiency \times acceptance evaluated with the nominal material budget conditions. For this reason the systematic uncertainty due to the material budget is estimated as:

$$\sigma_{\text{Mat.budget}}(p_T) = \frac{\varepsilon_{\text{max}}(p_T) - \varepsilon_{\text{min}}(p_T)}{\sqrt{12}}, \quad (9)$$

where $\varepsilon_{\text{max}}(p_T)$ and $\varepsilon_{\text{min}}(p_T)$ are the maximum and the minimum efficiency \times acceptance evaluated in each p_T interval. This formula represents the standard deviation of a uniform distribution assuming that ε_{max} and ε_{min} are its edges.

In the p_T region studied with the (anti-) ^3He analysis, instead, the variation of the material budget shows an uncertainty of the 3‰ and 2‰ of the estimated efficiency \times acceptance for the (anti-) ^3He and the ^3He respectively. This result is expected, as in that p_T region the detector acceptance for (anti-) ^3He in the rapidity region $|y| < 0.5$ is at its maximum and at the same time the (anti-) ^3He already reached its minimum of ionisation.

Another important check for the (anti-)nuclei analyses is the transport code adopted for the MC simulations. For the nuclei and especially the anti-nuclei under investigation in this work, the interaction cross sections have been measured in energy ranges far from the typical energies of light nuclei produced and measured in HIC [8, 9, 10, 11]. Therefore, the transport code has to interpolate between the measurements at lower and higher energies to get an estimation of the cross sections to be used in the propagation of the (anti-)nuclei in the material. The ALICE simulation framework supports the GEANT3 [12] and the GEANT4[13] transport codes, with GEANT3 used as the default transport code for simulations. Therefore an additional simulation using the GEANT4 transport code has been performed to check how much the efficiency \times acceptance varies. Figure 15 shows the efficiency \times acceptance corrections evaluated for (anti-)deuterons and (anti-) ^3He with GEANT3 and GEANT4. The MC production available at the time of this work are reproducing the detector configuration and running condition during the 2011 data taking. Since one could opt for either of the two and there is no guidance on which transport code is right in the determination of the efficiency \times acceptance, the systematic uncertainty evaluated with this check is the difference between the results obtained with the two transport codes divided by two.

This uncertainty accounts for the 8% and 10% of the estimated efficiency \times acceptance for nuclei and anti-nuclei respectively in the 2011 data sample. Since the detector configuration was changed before the start of the LHC Run 2 (e.g. the TRD installation was completed during the LHC shutdown) and no GEANT4 Monte Carlo is available for the Pb-Pb at $\sqrt{s_{\text{NN}}} = 5.02$ TeV, the systematic uncertainty used in the 2015 analysis is increased by 4% for both nuclei and anti-nuclei to cover the expected increase of this uncertainty with increasing material budget.

The track selection criteria variation is another powerful tool to inquire into all the effects that are either not properly described in the Monte Carlo sample (e.g. efficiency as a function of the number of selected clusters in the TPC) or not fully corrected in the analysis, like the secondary particle production from material contamination at low p_T for deuterons.

The selections shown in Table 3 are varied as described in the last column of Table 4.

For each of these selection variation the analyses are repeated *ab initio*. As changing the selection criteria varies the sample of (anti-)nuclei candidates analysed, only the statistically significant variations of the final results are kept into account in the systematic uncertainty variation. For the systematic

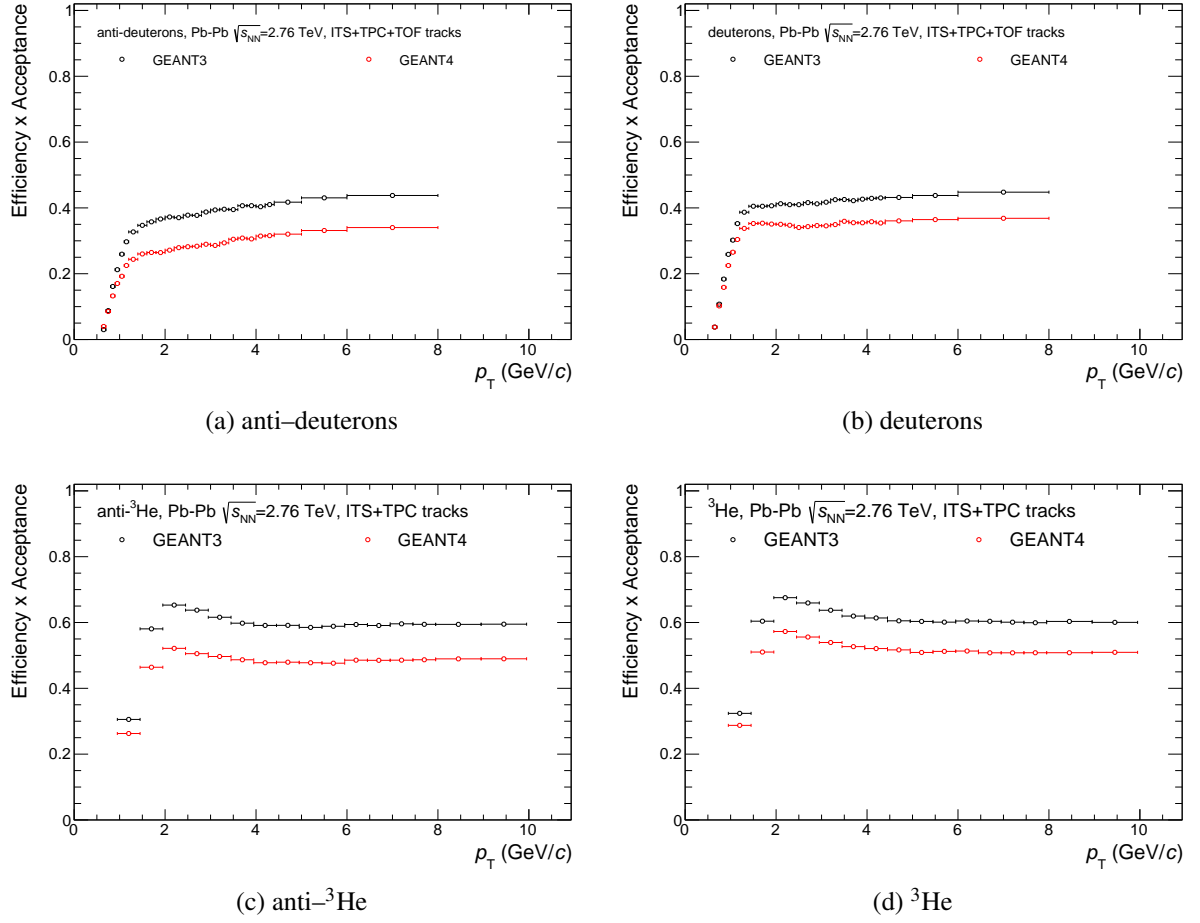


Fig. 15: Study of the effect of the transport code variation on the acceptance \times efficiency for (anti-)deuterons (top) and (anti-) ^3He (bottom). The MC simulations used were anchored to the 2011 data sample.

uncertainties estimation the results obtained by changing the track selections is then compared with the result attained with the nominal selections: only if the difference is more than 1σ the track selection variation is considered among the systematic uncertainties sources.

¹¹ For each selection criterion, the systematic uncertainty is evaluated as the standard deviation of the significant variations. The total systematic uncertainty due to the track selection variation is then the sum in quadrature of each of these contributions. One interesting feature that can be observed in the systematic uncertainty due to track variation (see the summary Figure 16) is the rise of the uncertainty at low p_T for deuteron. This rise comes from the variation of the DCA_z track selection: this particular selection is extremely sensitive to the contamination from secondary particles (see also [15]) and shows that the procedure to subtract them is not fully efficient when the contamination is more than approximately 85% (i.e. loose DCA_z track selection).

For (anti-) ^3He the statistical uncertainty is such that none of the track selection variation resulted in a significant variation of the final result, thus no systematic effect can be appreciated for the analysed data sample.

¹¹This is a quite general prescription in ALICE, going under the name of *Barlow criterion* from the paper by Roger Barlow [14].

Table 4: Track selection variations with respect to the standard selections quoted in Table 3 (replicated here in the column of the default values).

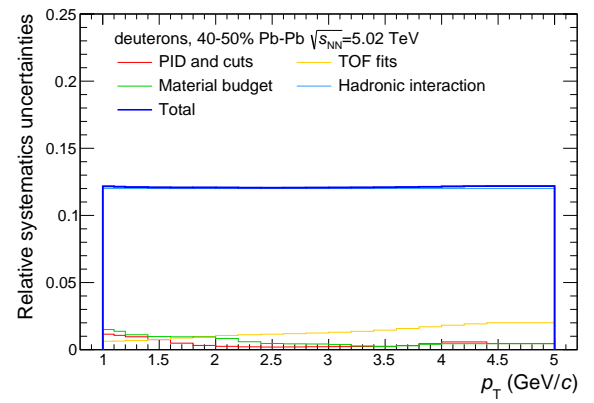
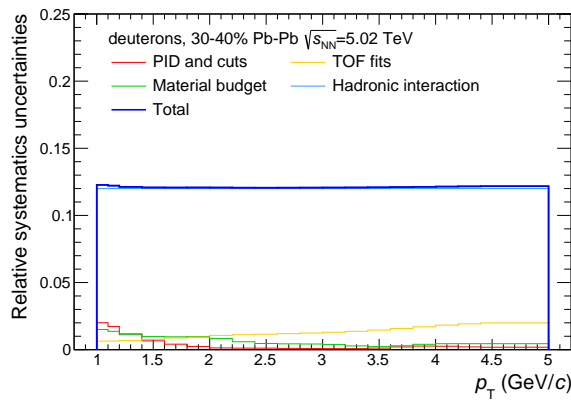
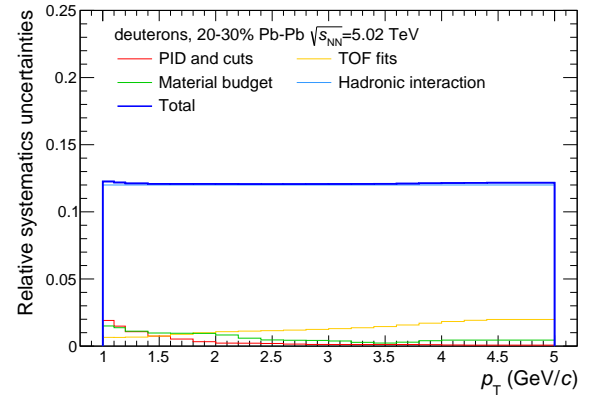
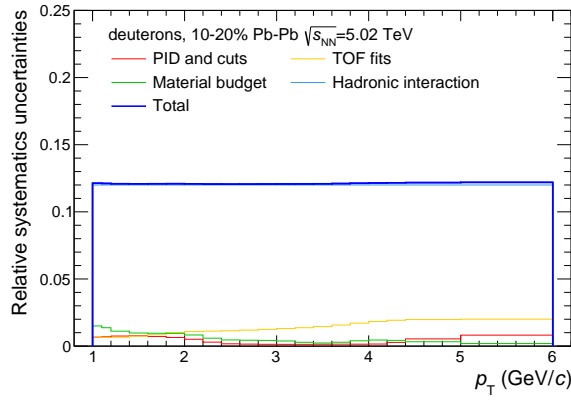
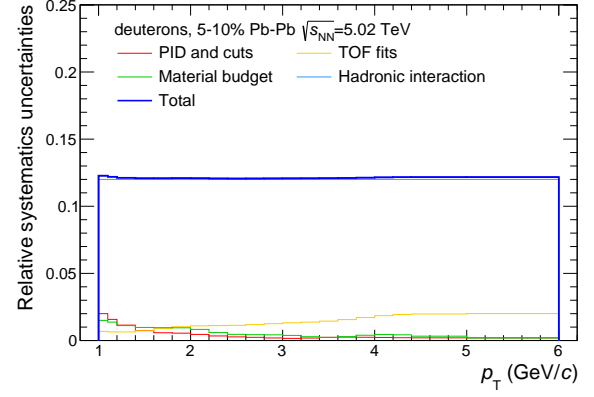
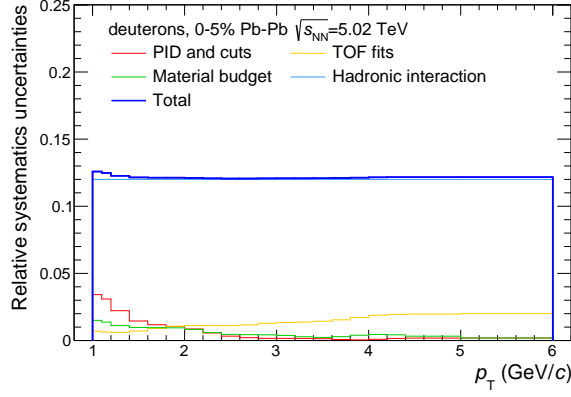
Description	Default values	Other values
# TPC clusters	70	60,65,75,80
$\chi^2/n_{\text{cl}}^{\text{TPC}}$	4	3.5,4.5,5.5,6
DCA _z (cm)	1	0.5,0.75,1.5,2
PID (σ_{TPC}), only for (anti-)d	3	2.5,3.5

The last systematic checks were done on the signal extraction for (anti-)deuterons and (anti-)³He. For (anti-)deuterons the systematic checks consisted in:

1. changing the fitting range using the same fit functions, having care that the fitting range was sufficiently wide not to cut any significant part of the signal. This has been attained by avoiding variations of the range in the region of 4σ from the mean of the signal, where σ is evaluated in the first fit;
2. changing the signal function to a simple Gaussian and keeping the same background shape;
3. changing the background function to the sum of an exponential and a polynomial of the first order.

The systematic uncertainty due to these variations is evaluated by computing their standard deviation. The summary Figures 16 and 17 show the trend of the evaluated fit systematic uncertainty in the 2011 and 2015 data samples respectively and in both cases the uncertainty rises with increasing p_T . This can be explained by the fact that also the signal over background ratio decreases with p_T making the signal extraction more challenging at the highest p_T interval.

For (anti-)³He the systematic checks on the signal extraction have been performed by varying the range in which the bin counting procedure is performed. While the standard range is between -3σ and 3σ , all the possible ranges between -3.5σ and 3.5σ have been checked. The tighter range used in this procedure is from -2.5σ to 2.5σ . The standard deviation of all these checks is taken as the systematic uncertainty of the signal extraction for (anti-)³He. Using this procedure the systematic uncertainty evaluated for (anti-)³He is less than the 3%, while for ³He, mainly because of the triton contamination subtraction at low p_T is as high as 2% (Table 5). Finally, the total systematic uncertainty has been computed summing in quadrature the contributions from all the checks mentioned above. For anti-³He the only significant contribution to the systematic uncertainty is coming from the transport codes and Table 5 summarises the outcome of the systematic checks for this species and for the ³He. For the other species studied here, Figure 16 and Figure 17 show the trend of the total systematic uncertainty, as well as of its components, as a function of the transverse momentum. In general, thanks to the better tracking performance of the ALICE experiment in the Run2 and a refined analysis strategy, the 2015 analysis shows smaller systematic uncertainties except for the difference between the transport code that needs a dedicated MC sample to be evaluated punctually.



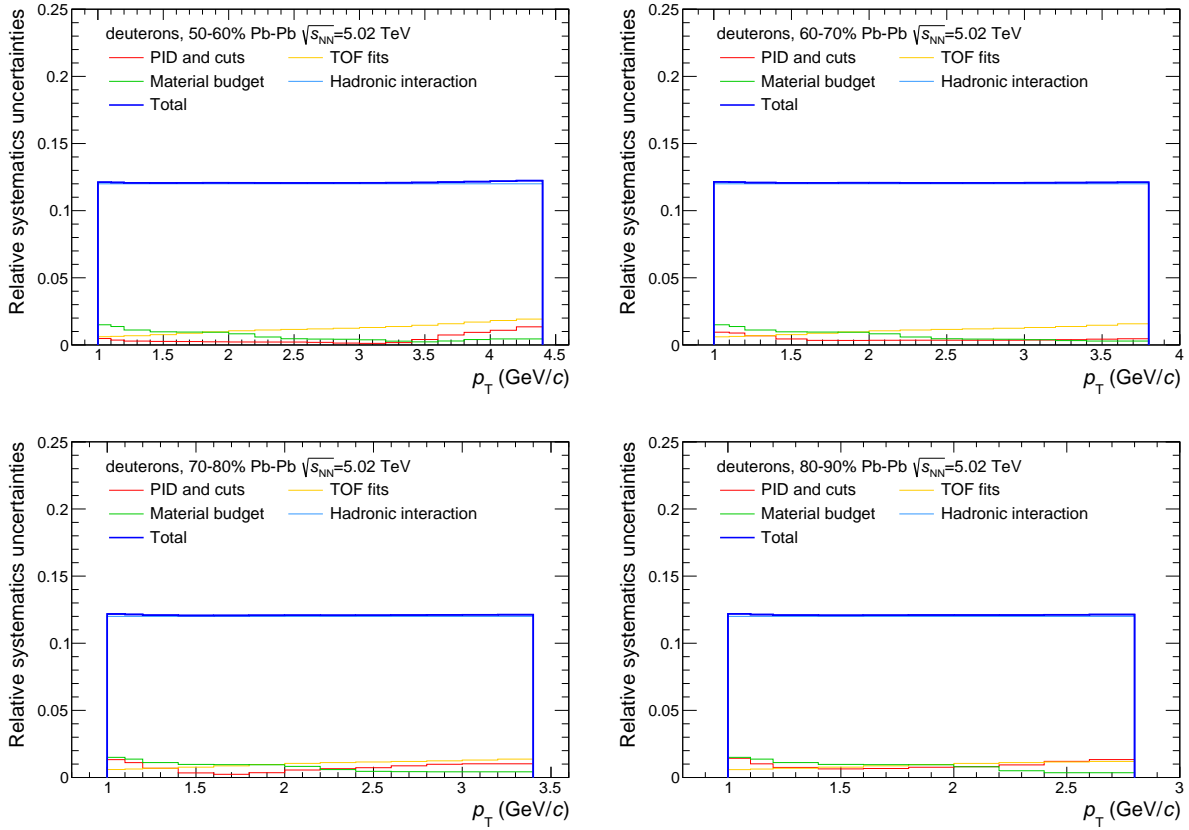
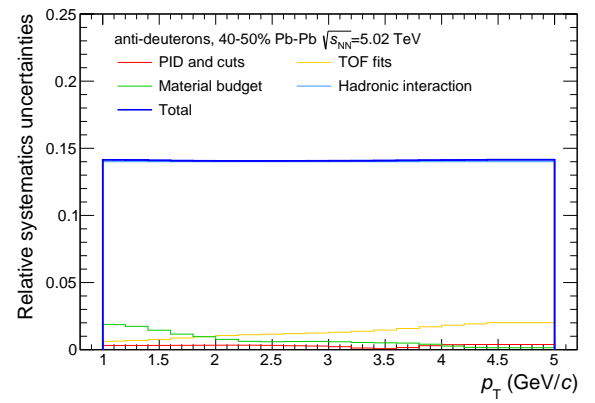
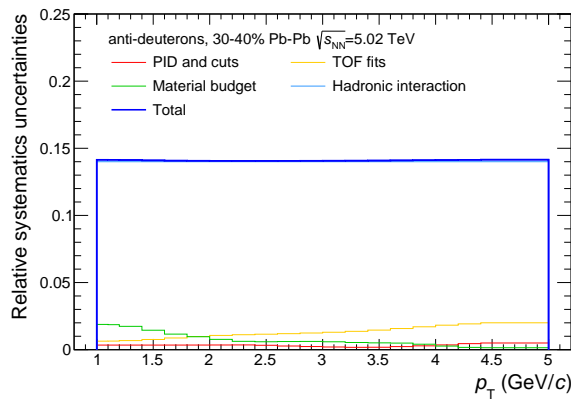
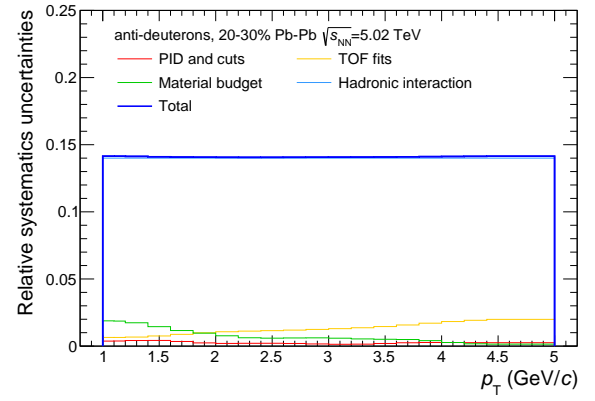
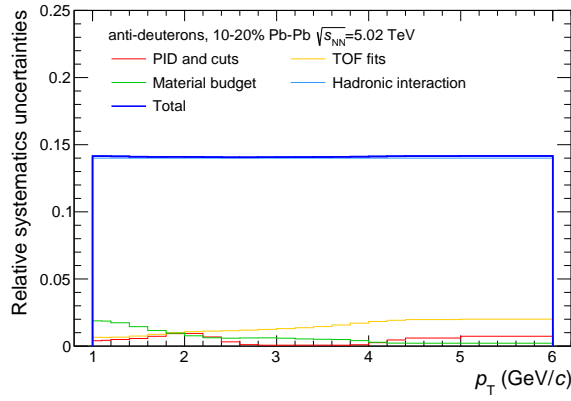
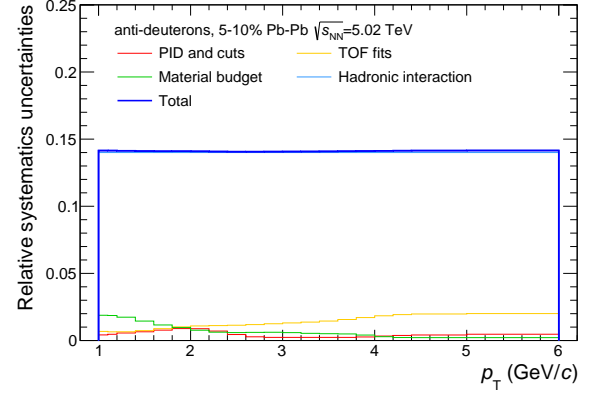
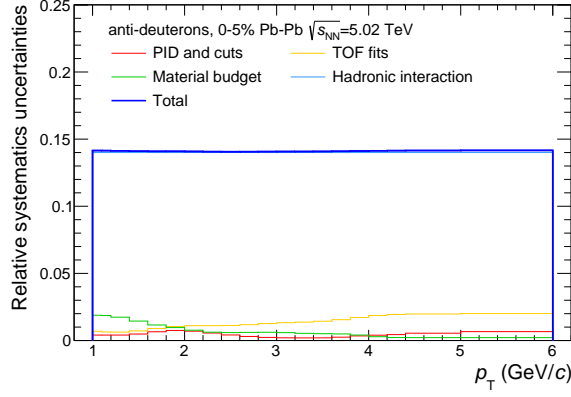


Fig. 16: Summary of the systematic uncertainties evaluated for the deuteron spectra in the different centrality classes of Pb–Pb at $\sqrt{s_{NN}} = 5.02$ TeV. The thick blue line represents the sum in quadrature of the systematic uncertainties contributions. The dominant uncertainty is the difference between the GEANT3 and GEANT4 transport codes (light blue line, called hadronic interaction), the TOF fits uncertainty (yellow line) follows. The PID and track selection variations (red line) show a pronounced peak at low p_T , because of the contamination from secondary particles. Also for the material budget variation (green line) the contribution is peaked at low p_T where the energy loss of the nuclei is higher.

Table 5: Summary of the systematic uncertainties contribution for the (anti-) ^3He analysis in the Pb–Pb at $\sqrt{s_{NN}} = 5.02$ TeV data sample. This table refers to all the centrality classes analysed in this thesis. The dominant contribution is the difference between the transport codes and for the anti- ^3He there are no other significant contributions. For the ^3He analysis, instead, the track selection and the signal extraction contribute marginally at low p_T , mainly due to the triton contamination in the TPC PID.

Contribution	anti- ^3He	^3He	
		$p_T = 2 \text{ GeV}/c$	$p_T \geq 4 \text{ GeV}/c$
Geant3/Geant4	14%	12%	
Track selections	$\leq 3\%$	$\approx 5\%$	$\leq 1\%$
Signal extraction	$\leq 2\%$	2%	$\leq 5\%$
Material budget	$\leq 4\%$	$\leq 2\%$	
Feed-down from (anti-) ^3H	5%	5%	



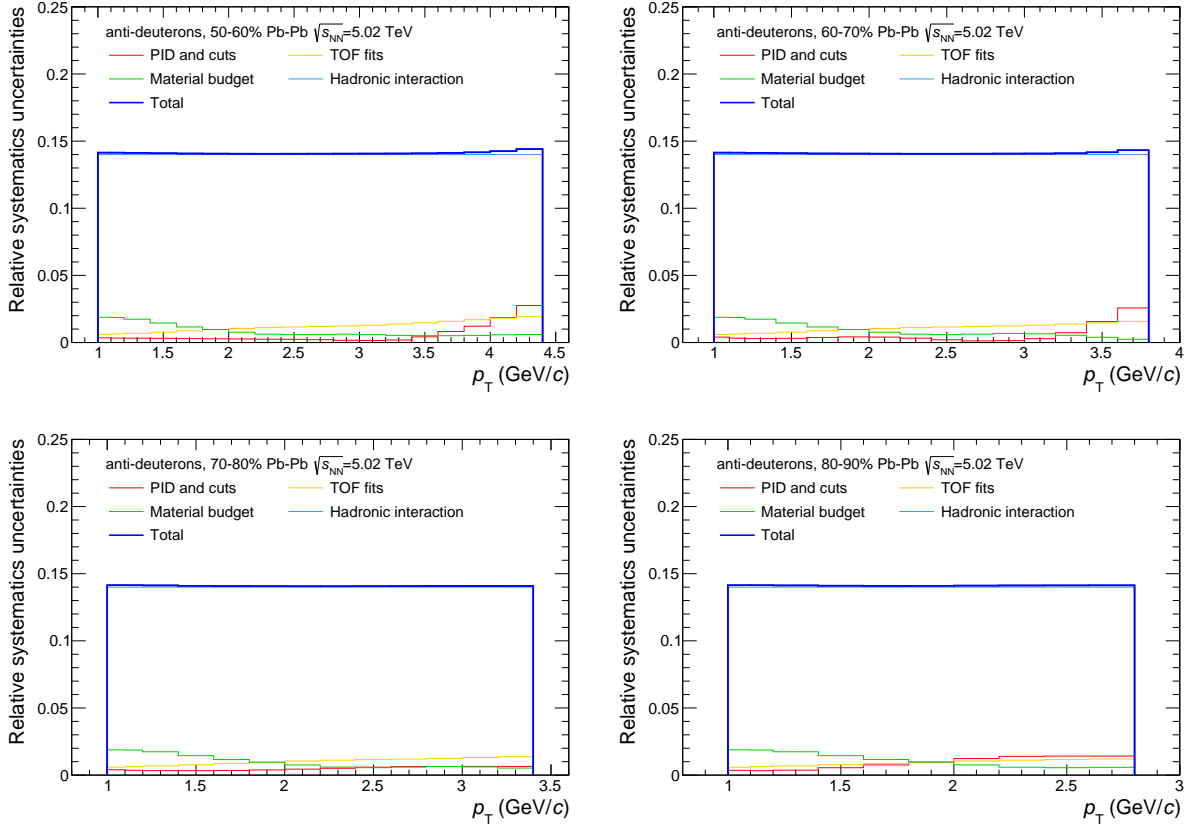


Fig. 17: Summary of the systematic uncertainties evaluated for the anti-deuteron spectra in the different centrality classes of Pb-Pb at $\sqrt{s_{NN}} = 5.02$ TeV. The thick blue line represents the sum in quadrature of the systematic uncertainties contributions. The dominant uncertainty is the difference between the GEANT3 and GEANT4 transport codes (light blue line, called hadronic interaction), the TOF fits uncertainty (yellow line) follows at high p_T . The material budget variation (green line) is peaked at low p_T where the energy loss of the nuclei is higher. Conversely the PID and track selection variations (red line) do not lead to a pronounced peak at low p_T , because of the lack of contamination from secondary particles for anti-deuterons, instead an enhancement of this contribution is visible around around $p_T = 2$ GeV/c where the TPC $n\sigma$ selection loses its effectiveness in rejecting the contamination from lighter particles.

2 Final results

The measurements of the (anti-)deuteron and (anti-) ^3He production spectra in Pb–Pb at $\sqrt{s_{\text{NN}}} = 5.02$ TeV will be discussed in this Section, together with an analysis of the integrated yields and mean transverse momentum of the spectra. Finally the results will be compared with the production of protons to inquire into the production mechanism of light nuclei in HIC.

2.1 Production spectra

Combining the information of the signal extraction and the corrections illustrated in the previous Chapter, the production spectra of light nuclei is evaluated as:

$$\frac{1}{N_{\text{ev}}} \frac{d^2N}{dy dp_T} = \frac{1}{N_{\text{ev}}} \frac{f_{\text{primary}}}{\varepsilon \cdot \varepsilon_{\text{G4/G3}}} \frac{dN_{\text{raw}}}{dp_T}, \quad (10)$$

where N_{ev} is the total number of events analysed for the measurement, ε is the acceptance \times efficiency correction, f_{primary} is the estimated fraction of primary particles and $\varepsilon_{\text{G4/G3}}$ is the correction due to the difference between GEANT3 and GEANT4 in the evaluation of the tracking efficiency.

Using this definition, it has been possible to measure the production spectra of (anti-)deuterons in Pb–Pb at the unprecedented energy of $\sqrt{s_{\text{NN}}} = 5.02$ TeV. The final spectra are shown in Figure 18. Thanks to the high number of events analysed in this new data sample, it has been possible to measure the spectra in finer centrality classes with respect to the published results [15] keeping, for the most central events, the same p_T reach obtained in the re-analysis of the Pb–Pb at $\sqrt{s_{\text{NN}}} = 2.76$ TeV (up to 6 GeV/c). Thanks to the finer centrality classes, it is possible to appreciate better the change of shape with the centrality of the spectra. This change indicates a modification of the properties of the expanding source as a function of the impact parameter. The same kind of qualitative observation applies to the (anti-) ^3He spectra measured on the new data sample and shown in Figure 19. The centrality classes definition in this case is statistically constrained by the low production yield of the ^3He and the number of collected events in 2015. Nevertheless, it has been possible to extend the measurements published in [15] adding one centrality class: the new centrality classes allow us to inquire into the differences among central (0-10%), semi-central (10-40%) and peripheral (40-90%) collisions in the (anti-) ^3He production.

Table 6: Ratio between matter and anti-matter for deuterons and ^3He in the Pb–Pb data sample at $\sqrt{s_{\text{NN}}} = 5.02$ TeV. The values were estimated by a weighted average of the ratios between anti-matter and matter production spectra. All the measured ratios are reported in the Appendix A.

Species	Centrality	Ratio
\bar{d}/d	0-5%	$0.99 \pm 0.00 \pm 0.04$
	5-10%	$0.98 \pm 0.00 \pm 0.04$
	10-20%	$0.97 \pm 0.00 \pm 0.04$
	20-30%	$0.98 \pm 0.00 \pm 0.04$
	30-40%	$1.00 \pm 0.00 \pm 0.04$
	40-50%	$1.03 \pm 0.00 \pm 0.04$
	50-60%	$1.00 \pm 0.01 \pm 0.05$
	60-70%	$0.99 \pm 0.01 \pm 0.05$
	70-80%	$0.99 \pm 0.02 \pm 0.05$
	80-90%	$0.89 \pm 0.04 \pm 0.07$
$^3\bar{\text{He}}/^3\text{He}$	0-10%	$0.89 \pm 0.04 \pm 0.08$
	10-40%	$0.97 \pm 0.03 \pm 0.08$
	40-90%	$1.02 \pm 0.06 \pm 0.10$

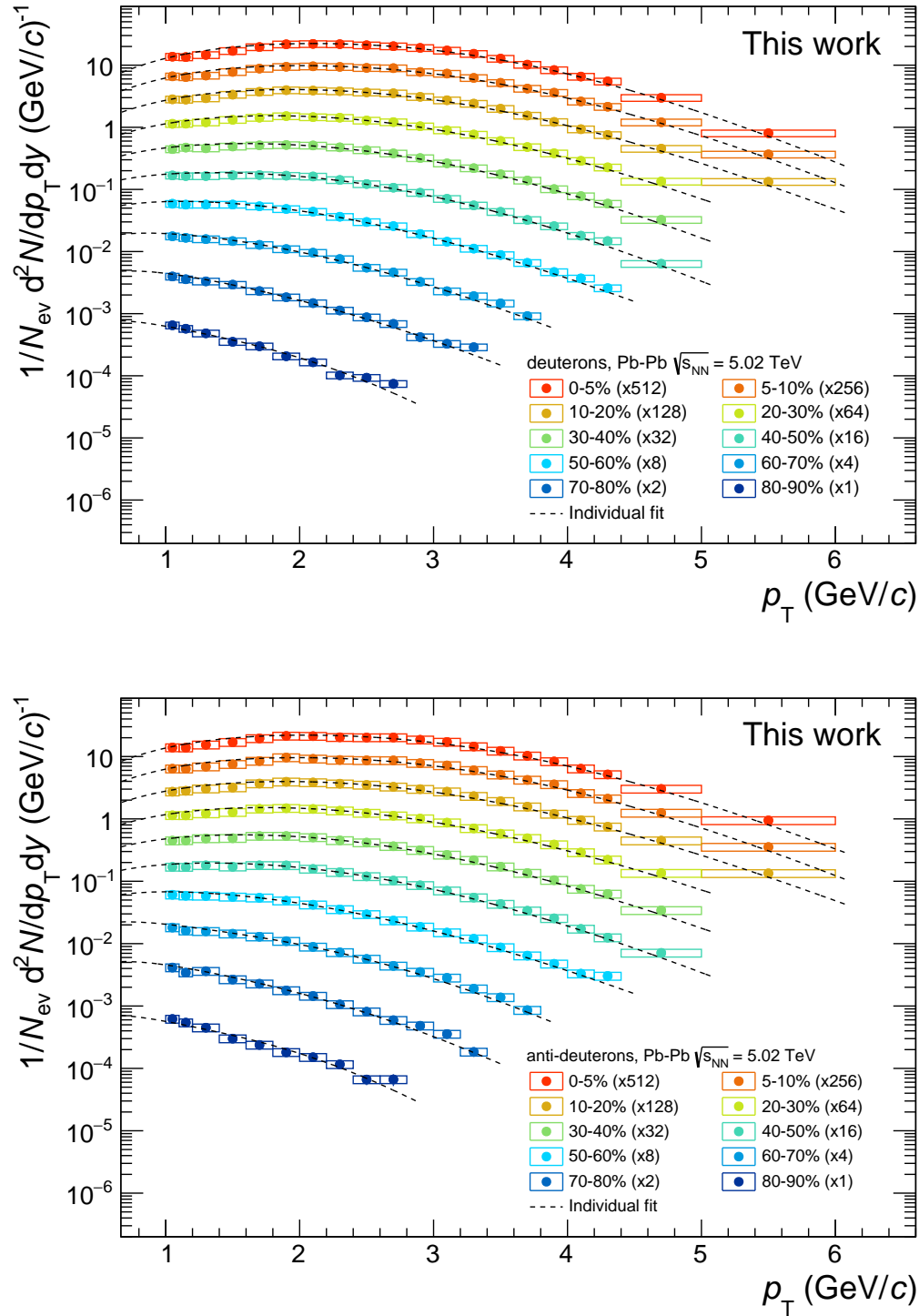


Fig. 18: Deuteron (top) and anti-deuteron (bottom) spectra measured in this analysis on the Pb-Pb at $\sqrt{s_{NN}} = 5.02$ TeV data sample. The boxes represent the systematic uncertainties while the vertical lines are the statistical ones. The dashed lines represent the individual Blast Wave fit to the spectra.

488 The anti-deuteron production spectra are compatible within the systematic and the statistical uncertainties
 489 with those of deuteron, as can be evicted from Table 6. The \bar{d}/d and ${}^3\text{He}/{}^3\text{He}$ ratios were estimated
 490 by a weighted average of the ratios between anti-matter and matter production spectra (see Appendix A).

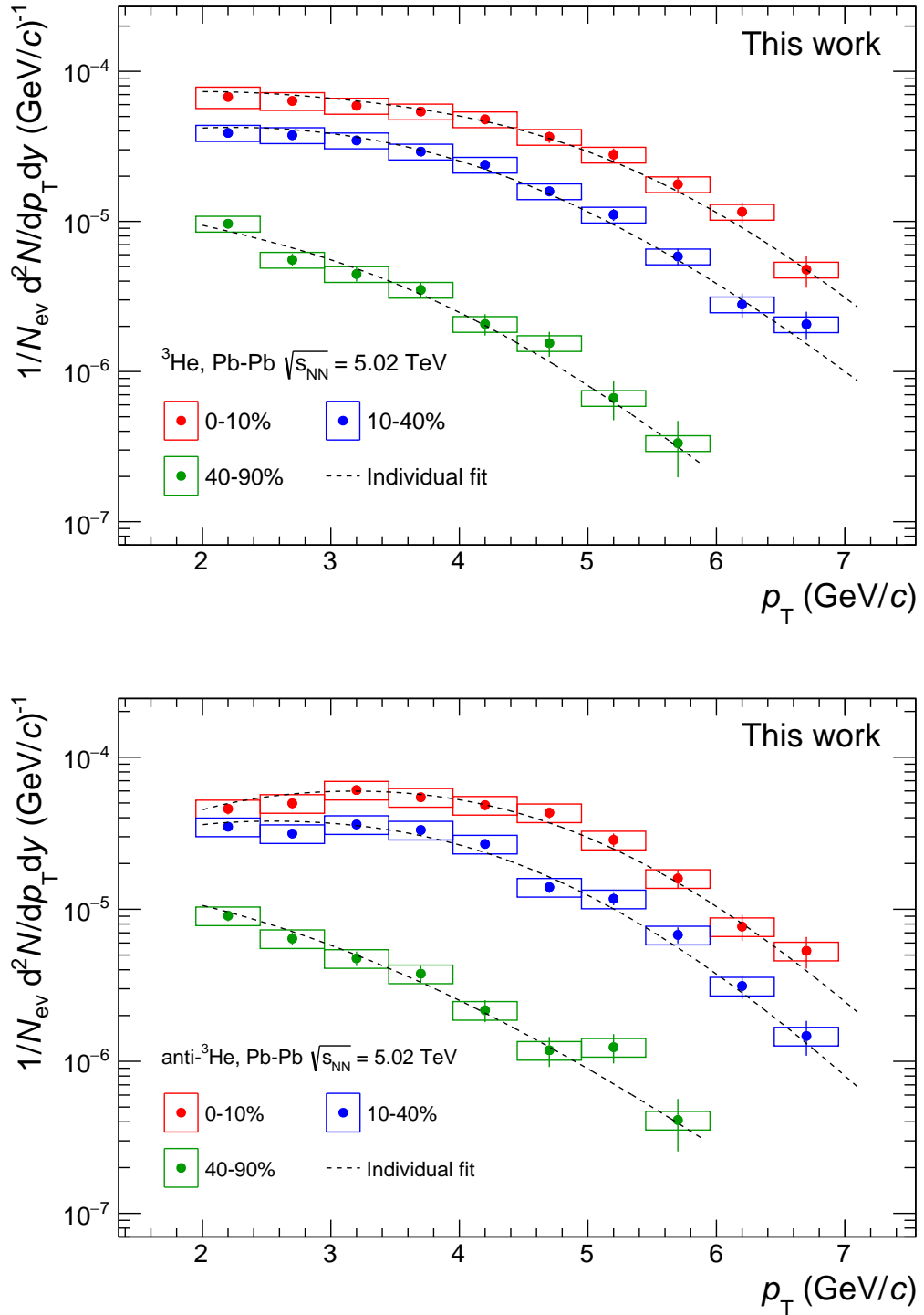


Fig. 19: ${}^3\text{He}$ (top) and anti- ${}^3\text{He}$ (bottom) spectra measured in this analysis on the Pb–Pb at $\sqrt{s_{NN}}=5.02$ TeV data sample. The boxes represent the systematic uncertainties while the vertical lines are the statistical ones. The dashed lines represent the individual Blast Wave fit to the spectra.

491 The statistical uncertainty is the error on the average of the p_T dependent ratio weighted with its statis-
 492 tical uncertainties. Similarly the systematic uncertainty has been evaluated with the same procedure but
 493 using as weights the systematic uncertainties of the p_T dependent ratio. In both coalescence and thermal

Table 7: Summary of the measured dN/dy and $\langle p_T \rangle$ for deuterons and ${}^3\text{He}$ in the centrality classes analysed in the Pb–Pb at $\sqrt{s_{\text{NN}}} = 5.02$ TeV data sample. The last column reports the χ^2/ndf for the Blast Wave fits to the spectra.

Centrality	dN/dy	$\langle p_T \rangle$ (GeV/c)	χ^2/ndf
d (0-5%)	$(1.19 \pm 0.00 \pm 0.21) \times 10^{-1}$	$2.45 \pm 0.00 \pm 0.09$	0.14
d (5-10%)	$(1.04 \pm 0.00 \pm 0.19) \times 10^{-1}$	$2.41 \pm 0.01 \pm 0.10$	0.17
d (10-20%)	$(8.42 \pm 0.02 \pm 1.50) \times 10^{-2}$	$2.34 \pm 0.00 \pm 0.11$	0.15
d (20-30%)	$(6.16 \pm 0.02 \pm 1.10) \times 10^{-2}$	$2.21 \pm 0.00 \pm 0.12$	0.08
d (30-40%)	$(4.25 \pm 0.01 \pm 0.75) \times 10^{-2}$	$2.05 \pm 0.00 \pm 0.12$	0.07
d (40-50%)	$(2.73 \pm 0.01 \pm 0.48) \times 10^{-2}$	$1.88 \pm 0.01 \pm 0.12$	0.09
d (50-60%)	$(1.62 \pm 0.01 \pm 0.28) \times 10^{-2}$	$1.70 \pm 0.01 \pm 0.11$	0.06
d (60-70%)	$(8.35 \pm 0.14 \pm 1.43) \times 10^{-3}$	$1.46 \pm 0.01 \pm 0.12$	0.16
d (70-80%)	$(3.52 \pm 0.06 \pm 0.63) \times 10^{-3}$	$1.27 \pm 0.02 \pm 0.11$	0.30
d (80-90%)	$(1.13 \pm 0.03 \pm 0.23) \times 10^{-3}$	$1.09 \pm 0.02 \pm 0.40$	0.39
${}^3\text{He}$ (0-10%)	$(2.70 \pm 0.13 \pm 0.59) \times 10^{-4}$	$3.06 \pm 0.09 \pm 0.34$	0.41
${}^3\text{He}$ (10-40%)	$(1.45 \pm 0.07 \pm 0.28) \times 10^{-4}$	$2.84 \pm 0.09 \pm 0.28$	0.69
${}^3\text{He}$ (40-90%)	$(3.18 \pm 0.30 \pm 0.59) \times 10^{-5}$	$1.99 \pm 0.12 \pm 0.11$	1.92

model frameworks, the obtained ratios are compatible with the expectation of a system with vanishing baryon chemical potential. If the μ_B of the system is null or close to zero, the number of nucleons and anti-nucleons in the system is the same and in the coalescence model there is no difference between the probability of producing a nucleus or an anti-nucleus. At the same time, in the thermal model approach the fugacity of a particle species $\lambda_i \propto e^{B_i \mu_B/T}$ (with B_i indicating the baryon number of the particle species) is the only different term in the expected total yields of baryons and anti-baryons. For vanishing chemical potential, the fugacities of nuclei and anti-nuclei coincide and their yields are the same according to the Statistical Hadronisation Models [16]. Quantitatively, both the statistical hadronization and the coalescence models predict that $\bar{d}/d = (\bar{p}/p)^2$ and ${}^3\bar{\text{He}}/{}^3\text{He} = (\bar{p}/p)^3$: this prediction is confirmed by the results of the present work when comparing them with the published \bar{p}/p measurements[17].

2.2 Yield and mean p_T

In order to measure the total yield per rapidity unit (dN/dy) of (anti-)deuterons and (anti-) ${}^3\text{He}$ and their average transverse momentum ($\langle p_T \rangle$), their spectra were fit with the Blast Wave function[18]. This function describes the measured spectra features assuming a thermal production of particles from an expanding source:

$$\frac{1}{p_T} \frac{dN}{dp_T} \propto \int_0^R r m_T I_0 \left(\frac{p_T \sinh \rho}{T_{\text{kin}}} \right) K_1 \left(\frac{m_T \cosh \rho}{T_{\text{kin}}} \right) dr, \quad (11)$$

where I_0 and K_1 are the modified Bessel functions, r is the distance from the centre of the expanding system, R is the limiting radius of the system expansion, T_{kin} is the temperature of the kinetic freeze-out and ρ is the velocity profile. The velocity profile can be expressed in terms of the transverse expansion velocity at the system surface, β_S , and an exponent n :

$$\rho = \tanh^{-1} [\beta_S (r/R)^n]. \quad (12)$$

Since the production spectra of nuclei and anti-nuclei are compatible and the anti-nuclei spectra are affected by larger systematic uncertainties, the measurement of the yield is performed using the nuclei spectra only. The Blast-Wave function was used to extract the central value and the statistical uncertainties of the dN/dy and $\langle p_T \rangle$, but the systematic uncertainty due to the extrapolation in the unmeasured region at high and low transverse momenta was evaluated by fitting the spectrum using three additional functions:

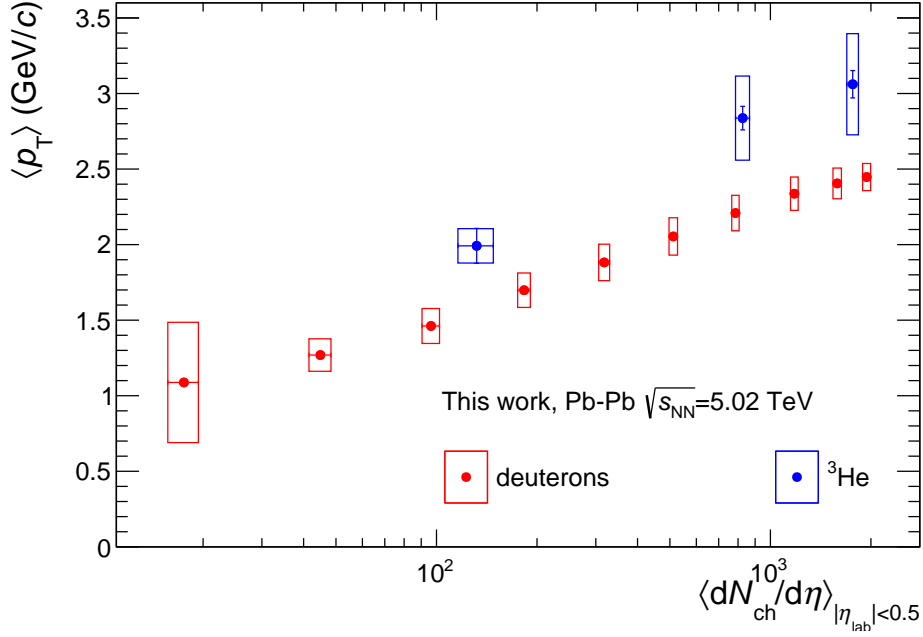


Fig. 20: Mean transverse momentum for deuterons (red) and ^3He (blue) as a function of the measured charged particle multiplicity in the pseudorapidity region $|\eta| < 0.5$. The vertical lines and the boxes represent the statistical and systematic uncertainties respectively.

519 1. an m_T exponential function

$$\frac{dN}{dp_T dy} = A e^{-m_T/T}, \quad (13)$$

520 with A and T as fit parameters;

521 2. a Levy–Tsallis model[19]

$$\frac{1}{p_T} \frac{dN}{dp_T dy} = \frac{dN}{dy} \frac{(n-1)(n-2)}{nC[nC+m(n-2)]} \left(1 + \frac{m_T - m}{nC}\right)^{-n}, \quad (14)$$

522 with C , n and the dN/dy as fit parameters and m the mass of the particle under study;

523 3. a Boltzmann distribution

$$\frac{dN}{dp_T dy} = A p_T m_T e^{-m_T/T}, \quad (15)$$

524 with A and T as fit parameters.

525 Half of the difference between the maximum and the minimum dN/dy and p_T computed with the differ-
 526 ent functions was added in quadrature to the systematic uncertainty. The latter was evaluated by fitting
 527 the Blast Wave function to the spectrum shifted up and down by a factor equal to its systematic uncer-
 528 tainty. The difference between the different fit functions is the dominant contribution to the systematic
 529 uncertainty in the case of the ^3He spectra and the spectra of deuterons in peripheral events (from 70%
 530 to 90%) because of the limited p_T coverage of the analysis. The measured $\langle p_T \rangle$ and dN/dy with their
 531 statistical and systematic uncertainties are shown in Table 7.

532 Figure 20 shows the evolution of the $\langle p_T \rangle$ with the average charged particles density in the pseudorapidity
 533 region $|\eta| < 0.5$, that is a proxy for the centrality of the collision. The centrality classes adopted in the

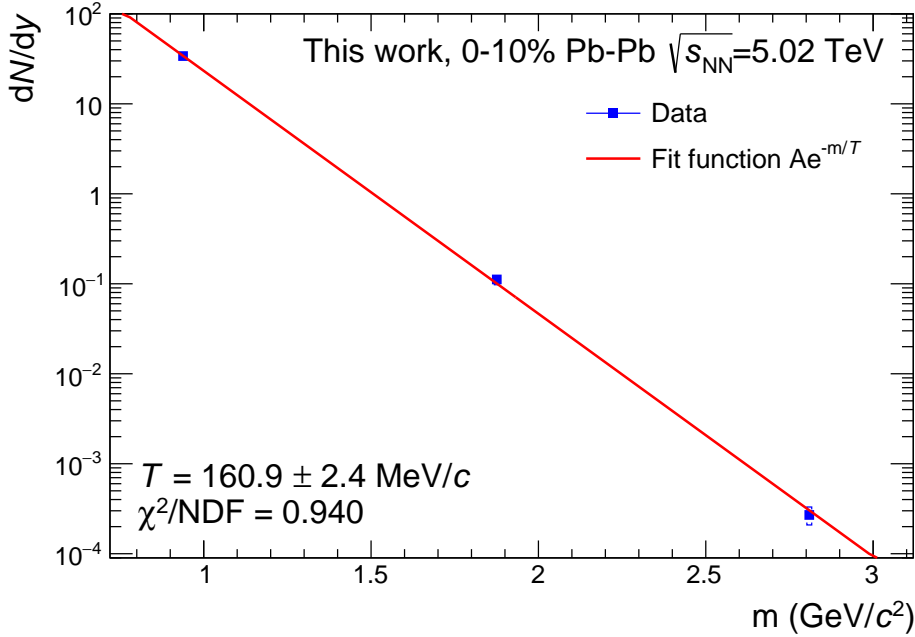


Fig. 21: Distribution of the dN/dy of protons, deuterons and ${}^3\text{He}$ as a function of their mass for the Pb–Pb data sample at $\sqrt{s_{NN}}=5.02$ TeV. The red line shows the fit to this distribution with the exponential law expected by a simplified approach to the thermal model.

extraction of the spectra were translated in $\langle dN/d\eta \rangle$ using the values tabulated in [20]. The rise of the mean transverse momentum with the centrality confirms the trend observed for the other particle species because of the presence of stronger pressure gradients in the system created in HIC generating a stronger *radial flow*. The relevance of radial flow is also often highlighted by the presence of a mass ordering of the $\langle p_T \rangle$: this phenomenology is visible also in the case of the light nuclei where the ${}^3\text{He}$ (i.e. the heavier between ${}^3\text{He}$ and deuterons) has the highest mean transverse momentum when comparing similar centralities (Figure 20).

2.3 Comparisons to the theoretical expectations

As already highlighted in the previous section, the fugacity of a particle species is steering its production yield. Since the ratio between the baryons and the anti-baryons production is compatible with unity in HIC at the LHC, the fugacity is (very close to) 1 for nucleons and light nuclei. In a simplistic approach within the SHM framework, the production yield of protons, deuterons and ${}^3\text{He}$ should follow

$$\left(\frac{dN}{dy} \right)_{\text{nuc.}} \propto e^{-m/T_{\text{chem}}}, \quad (16)$$

where m is the mass of the nucleon(us) and T_{chem} is the temperature of the chemical freeze-out.¹² Figure 21 shows the dN/dy of protons¹³, deuterons and ${}^3\text{He}$ in the 0-10% centrality class of the Pb–Pb at $\sqrt{s_{NN}}=5.02$ TeV data sample as a function of their mass. The exponential function 16 fits the data with a good reduced χ^2 and with parameters compatible with those shown in [15]. Thanks to the result of this exponential fit it is also possible to predict the expected dN/dy of heavier nuclei, knowing that adding an additional nucleon to a nucleus will cost a penalty factor of approximately 300 to its dN/dy .

¹²This approach neglects many caveats of the statistical hadronisation model, for instance the different eigen-volume correction for different particle species and the resonance feed-down.

¹³The dN/dy of protons, as well as the spectra that will be used later, were taken by the recently released preliminary analysis of the ALICE experiment [21, 5].

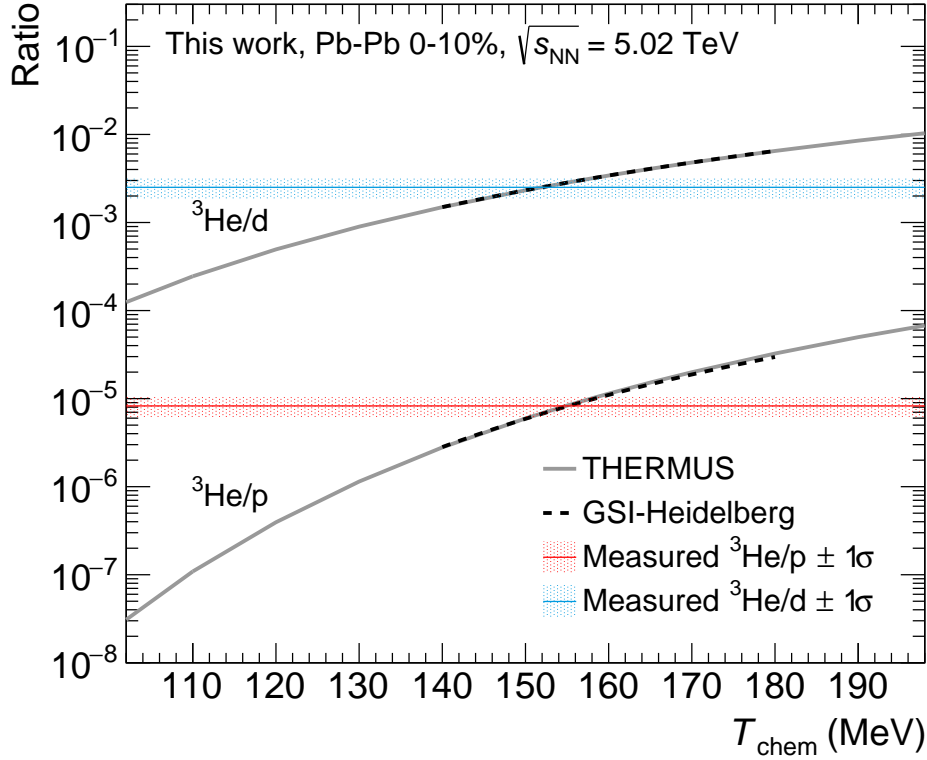


Fig. 22: Measured ${}^3\text{He}$ over deuteron ratio (blue line) and ${}^3\text{He}$ over proton ratio (red line) compared with the predictions of the THERMUS (grey line, [22]) and GSI-Heidelberg (dashed line, [16]) SHM models. The shaded areas correspond to the 1σ uncertainty (statistical + systematic) interval from the measurements.

In the thermal model framework, the yield of a particle species i , $\langle N_i \rangle$, is proportional to the volume of the system V . It is possible to eliminate the dependence on the system volume studying the ratio between the yield of different particle species. In this way it is possible to investigate directly the chemical freeze-out temperature of the system. Figure 22 shows the comparison between the measured ${}^3\text{He}$ over deuteron (blue line) and ${}^3\text{He}$ over proton ratios (red line) and the prediction from two different implementation of the SHM [16, 22, 23] as a function of the chemical freeze-out momentum. The range of chemical freeze-out temperatures compatible within 1σ with the measurements is between 150 and 158 MeV, that is very close to the temperature attained with the simplistic approach used in Figure 21.

The other class of models for the production of (anti-)nuclei in HIC can be investigated by computing the coalescence parameters B_2 and B_3 for deuterons and ${}^3\text{He}$ respectively:

$$B_A = E_i \frac{d^3 N_i}{dp_i^3} \left(E_p \frac{d^3 N_p}{dp_p^3} \right)^{-A}. \quad (17)$$

The definition adopted in the models uses the proton spectra before the formation of the nuclei. The experimental computation of the coalescence parameters relies on the fact that the production of nuclei with mass number A is suppressed by a factor of $(300)^{-A}$ with respect to the proton yield. Therefore, the proton spectrum used in the coalescence model can be replaced by the measured proton spectrum. Figure 23 shows the measured coalescence parameters B_2 and B_3 as a function of the transverse momentum scaled by the mass number A for Pb–Pb collisions at $\sqrt{s_{NN}} = 5.02$ TeV. From this Figure it is possible to see an ordering of the coalescence parameters with the centrality, going from higher B_A values in peripheral collisions to lower B_A values in the central ones. As illustrated in the introduction Chapter,

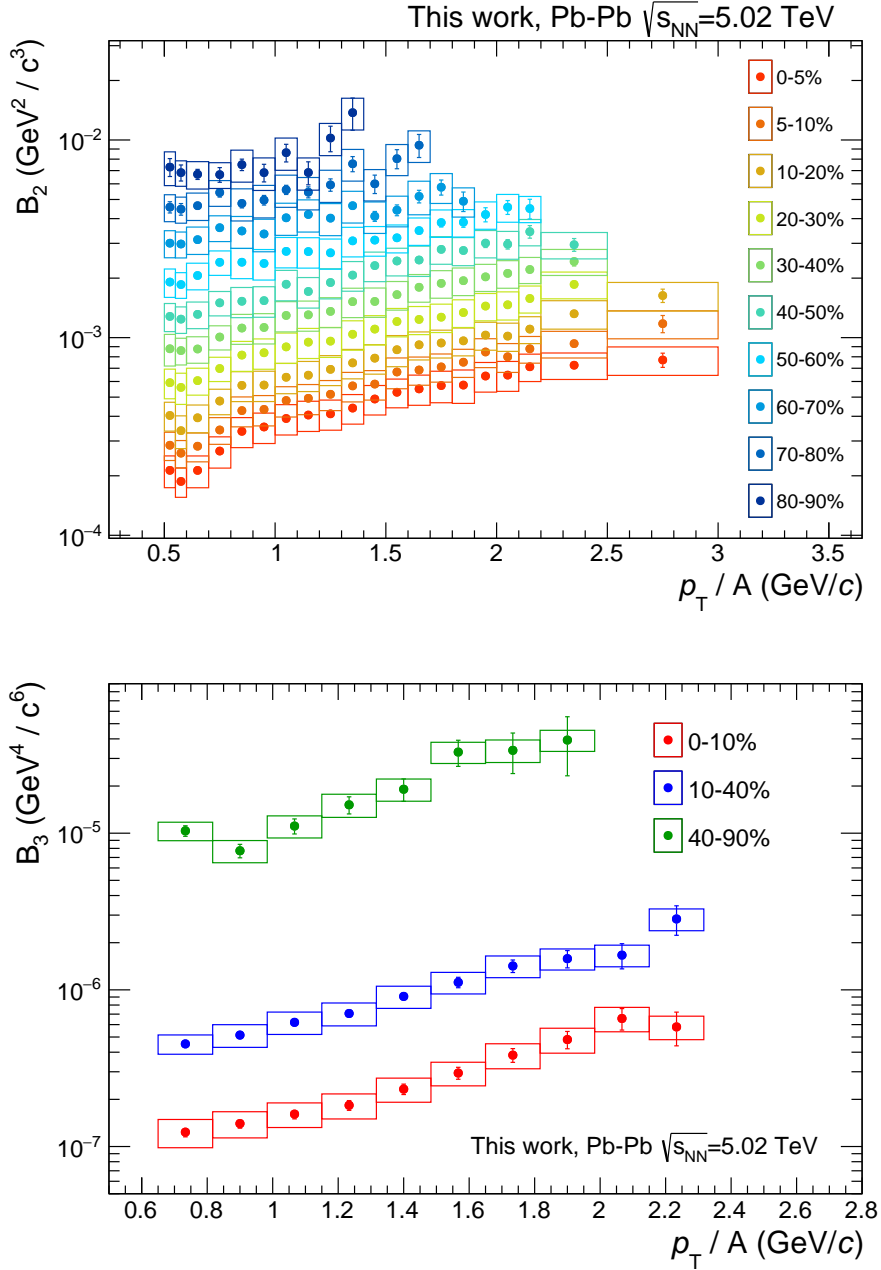


Fig. 23: Coalescence parameters B_2 (top) and B_3 (bottom) measured in Pb–Pb collisions at $\sqrt{s_{NN}} = 5.02$ TeV as a function of the transverse momentum scaled by the mass number of the nucleus. Each colour corresponds to a different centrality class. See the text for details.

570 this trend with centrality is explained in the coalescence model framework as an increasing volume V_{eff}
 571 of the source going from peripheral to central events. If the V_{eff} is bigger, the probability of having
 572 two nucleons close enough in the phase space to form a bound state is lower, thus the coalescence
 573 parameters are smaller. In addition, the measured coalescence parameters show a significant increase
 574 with the transverse momentum that is not explained by the simplest formulation of the coalescence
 575 models. One possible extension to the model, briefly described in the introduction Chapter and in [24],
 576 explains the observed trend by assuming a smaller emission radius, thus a smaller V_{eff} , for particles
 577 with higher and higher momentum. Alternatively, as outlined in [15], a qualitative explanation for this
 578 trend can be found by taking into account the position–momentum correlation induced by an expanding

579 thermal source [25]. Nevertheless, at the time of this work there are no quantitative predictions in the
 580 coalescence model framework that can be compared with the results obtained in this work.

581 2.4 Nucleus over proton ratio

582 In the HIC, the evolution with centrality, and in general with the charged particle multiplicity, of the ratio
 583 between nuclei and protons dN/dy defined as

$$R(A) = \frac{(dN/dy)_A}{(dN/dy)_p} \quad (18)$$

584 it is a benchmark for the models of the nuclei production mechanism. According to the thermal model
 585 interpretation, $R(A)$ is fixed by the temperature of the source, thus it has to stay constant with the charged
 586 particle multiplicity evolution. On the other hand, in a naive coalescence picture $R(A)$ should increase
 587 with the multiplicity of nucleons produced in the collision. The $R(A)$ ratio as a function of multiplicity
 588 published in [15] was found to be independent of the charged particle multiplicity. The published ratio
 589 was compatible with the thermal model prediction with a chemical freeze-out temperature between 150
 590 and 160 MeV [15]. Figure 24 shows $R(2)$ for deuterons (top pad) and $R(3)$ ^3He (bottom pad). In both
 591 cases the measurement presented in this work represents a substantial extension of the multiplicity range
 592 covered in this kind of analysis. In the case of the ^3He over proton ratio, the result obtained in this work
 593 is compatible, within uncertainties, with that shown in [15]. This ratio does not exhibit any evident trend
 594 with the multiplicity, confirming the picture sketched by the thermal model predictions. Conversely the
 595 deuteron over proton ratio shows a deviation from the constant behaviour. In the region of overlap with
 596 the results shown in [15], the ratio computed in this work is compatible with that obtained in Pb–Pb
 597 collisions at $\sqrt{s_{NN}}=2.76$ TeV. Furthermore an important point is that, thanks to the analysis carried out
 598 in the present work, it was possible to have a quantitative comparison with preliminary results in p–
 599 Pb collisions. Indeed, at low charged particle multiplicity the ratio for Pb–Pb starts to decrease and it
 600 overlaps with the p–Pb results. Similarly, at high multiplicity it is possible to see a hint of suppression of
 601 the deuteron production with respect to protons. One possible explanation of the observed pattern can be
 602 found in [26], where the similar trend observed in the Ξ over pion ratio is explained as a consequence of
 603 the different rescattering conditions after the chemical freeze-out. In that context, the depletion at very
 604 central collision is interpreted as an increased number of interactions in the rescattering phase, moving
 605 the observed yield away from the chemical equilibrium. While at low multiplicity, *corona* effects[27]
 606 lead to a depletion of the deuteron over proton ratio going toward the value observed in pp collisions.

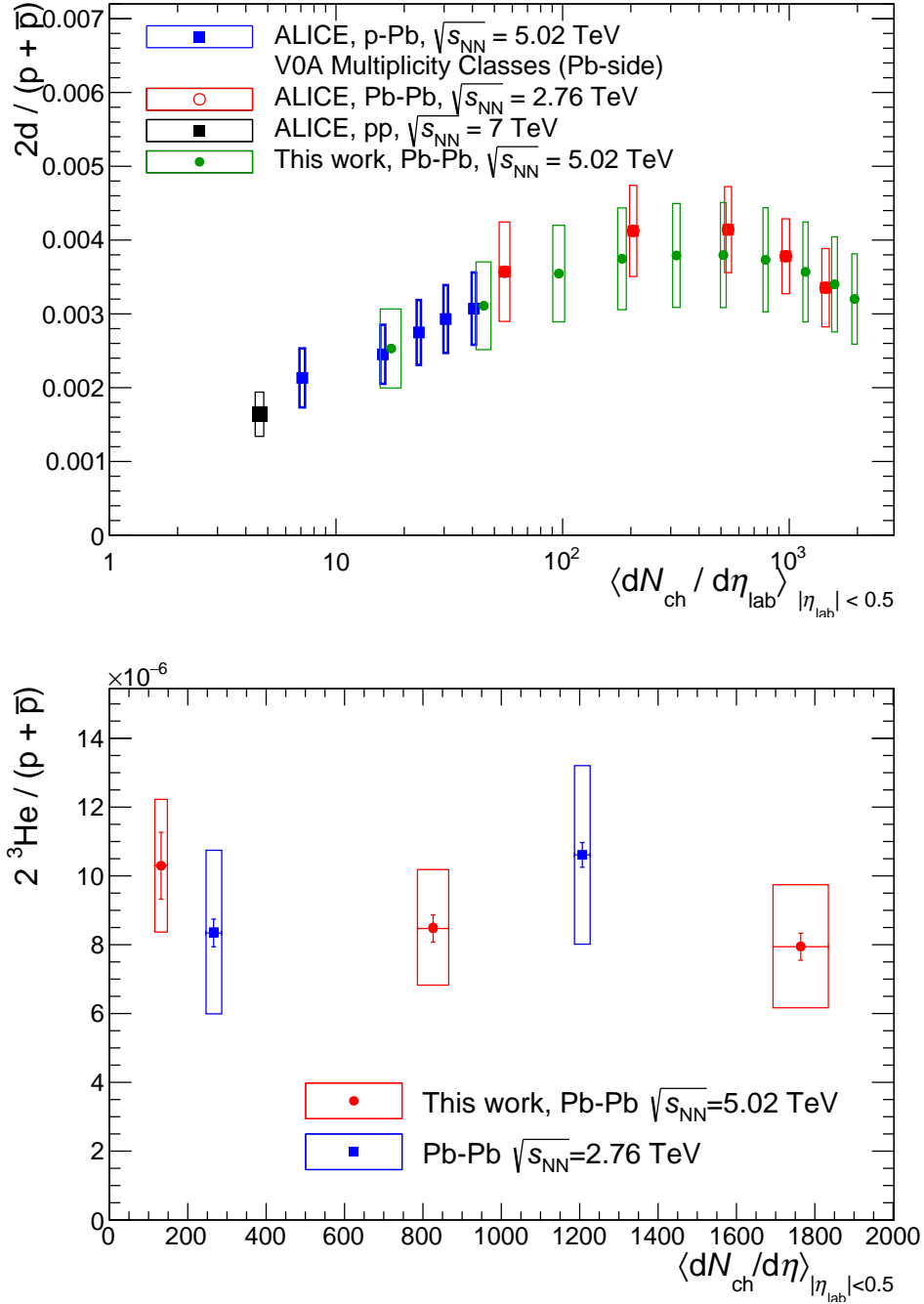


Fig. 24: Ratio between the measured dN/dy of nuclei and proton as a function of the charged particle multiplicity. The vertical lines represent the statistical uncertainties while the boxes represent the systematic ones. The top pad shows the results for d/p ratio obtained in this work (green points) compared with those published in [15] (red points for Pb–Pb and black dot for pp) and the preliminary results of ALICE in p–Pb collisions [23] (blue points). The bottom pad shows the $^3\text{He}/p$ ratio measured in this work (blue points) compared with those published (red dots).

607 A Ratios anti-nuclei over nuclei

608 In this appendix the ratios between the anti-nuclei and the nuclei spectra are shown as a function of the
 609 transverse momentum and in all the centrality classes analysed in this work.

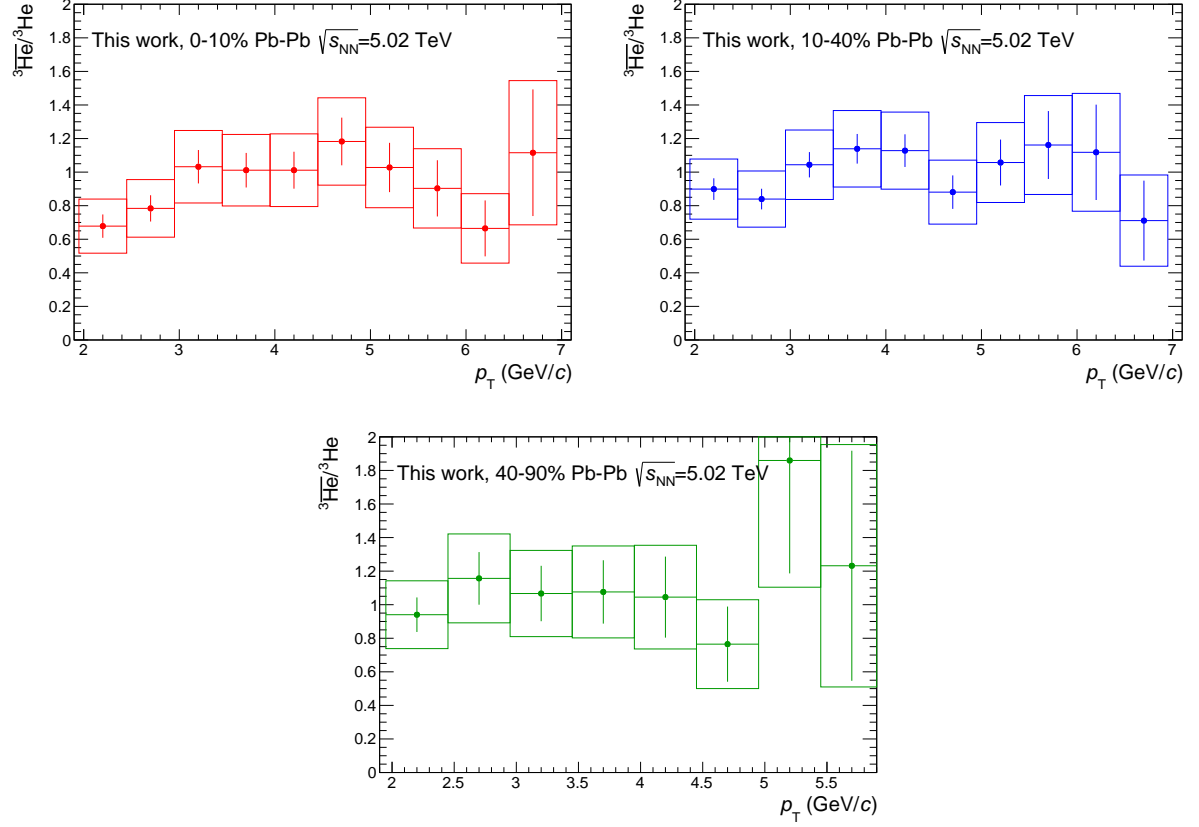
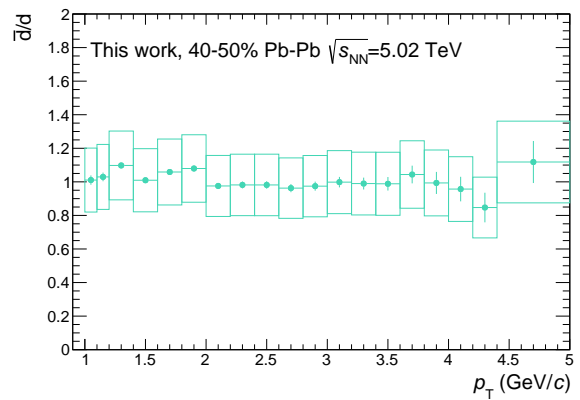
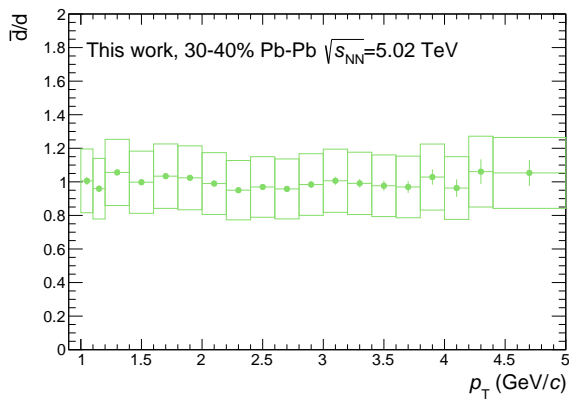
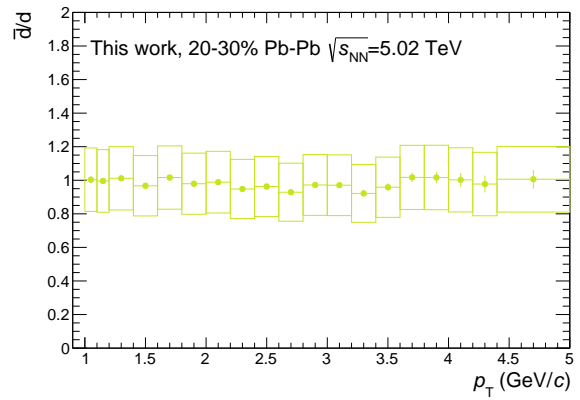
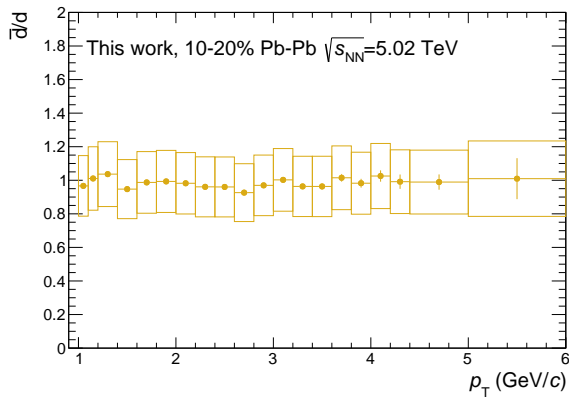
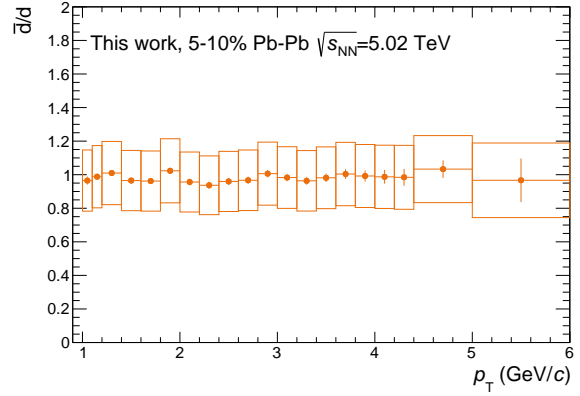
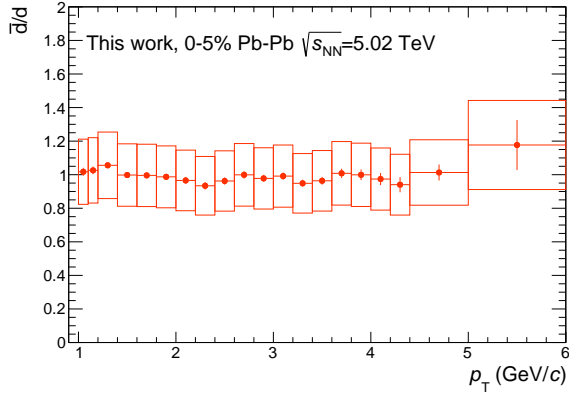


Fig. A.1: Ratio between the ${}^3\bar{\text{He}}$ and the ${}^3\text{He}$ spectra for all the centrality classes covered in this work for the Pb–Pb at $\sqrt{s_{NN}}=5.02$ TeV data sample.



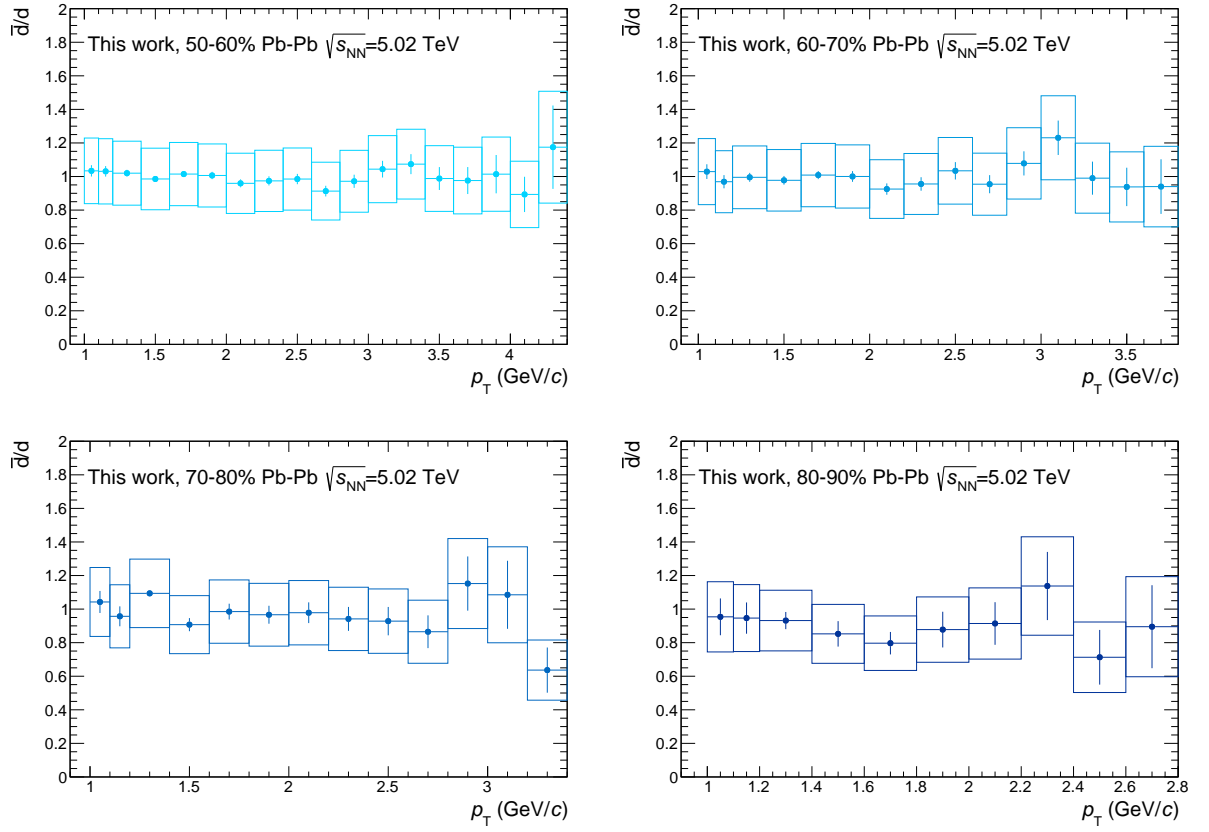


Fig. A.2: Ratio between the anti-deuteron and the deuteron spectra for all the centrality classes covered in this work for the Pb–Pb at $\sqrt{s_{NN}}=5.02$ TeV data sample.

References

- [1] B. Abelev *et al.*, “Centrality determination of Pb-Pb collisions at $\sqrt{s_{NN}} = 2.76$ TeV with ALICE,” *Phys. Rev.*, vol. C88, no. 4, p. 044909, 2013.
- [2] X.-N. Wang and M. Gyulassy, “HIJING: A Monte Carlo model for multiple jet production in p p, p A and A A collisions,” *Phys. Rev.*, vol. D44, pp. 3501–3516, 1991.
- [3] B. B. Abelev *et al.*, “Performance of the ALICE Experiment at the CERN LHC,” *Int. J. Mod. Phys.*, vol. A29, p. 1430044, 2014.
- [4] J. Adam *et al.*, “ ${}^3_{\Lambda}\text{H}$ and ${}^3_{\Lambda}\bar{\text{H}}$ production in Pb-Pb collisions at $\sqrt{s_{NN}} = 2.76$ TeV,” *Phys. Lett.*, vol. B754, pp. 360–372, 2016.
- [5] N. Jacazio. Private communication.
- [6] M. Puccio, “RooCustomPdfs.” <https://github.com/mpuccio/RooCustomPdfs>, 2016.
- [7] R. J. Barlow and C. Beeston, “Fitting using finite Monte Carlo samples,” *Comput. Phys. Commun.*, vol. 77, pp. 219–228, 1993.
- [8] A. Auce, R. F. Carlson, A. J. Cox, A. Ingemarsson, R. Johansson, P. U. Renberg, O. Sundberg, and G. Tibell, “Reaction cross-sections for 38, 65, and 97 MeV deuterons on targets from Be-9 to Pb-208,” *Phys. Rev.*, vol. C53, pp. 2919–2925, 1996.
- [9] F. G. Binon *et al.*, “Absorption cross-sections of 25 gev/c antideuterons in li, c, al, cu and pb,” *Phys. Lett.*, vol. 31B, pp. 230–232, 1970.
- [10] J. Jaros *et al.*, “Nucleus-Nucleus Total Cross-Sections for Light Nuclei at 1.55-GeV/c/Nucleon and 2.89-GeV/c/Nucleon,” *Phys. Rev.*, vol. C18, pp. 2273–2292, 1978.
- [11] S. P. Denisov, S. V. Donskov, Yu. P. Gorin, V. A. Kachanov, V. M. Kutjin, A. I. Petrukhin, Yu. D. Prokoshkin, E. A. Razuvaev, R. S. Shuvalov, and D. A. Stojanova, “Measurements of anti-deuteron absorption and stripping cross sections at the momentum 13.3 gev/c,” *Nucl. Phys.*, vol. B31, pp. 253–260, 1971.
- [12] R. Brun, R. Hagelberg, M. Hansroul, and J. C. Lassalle, *Simulation program for particle physics experiments, GEANT: user guide and reference manual*. Geneva: CERN, 1978.
- [13] S. Agostinelli *et al.*, “GEANT4: A Simulation toolkit,” *Nucl. Instrum. Meth.*, vol. A506, pp. 250–303, 2003.
- [14] R. Barlow, “Systematic errors: Facts and fictions,” in *Advanced Statistical Techniques in Particle Physics. Proceedings, Conference, Durham, UK, March 18-22, 2002*, pp. 134–144, 2002.
- [15] J. Adam *et al.*, “Production of light nuclei and anti-nuclei in pp and Pb-Pb collisions at energies available at the CERN Large Hadron Collider,” *Phys. Rev.*, vol. C93, no. 2, p. 024917, 2016.
- [16] A. Andronic, P. Braun-Munzinger, J. Stachel, and H. Stocker, “Production of light nuclei, hyper-nuclei and their antiparticles in relativistic nuclear collisions,” *Phys. Lett.*, vol. B697, pp. 203–207, 2011.
- [17] B. Abelev *et al.*, “Centrality dependence of π , K, p production in Pb-Pb collisions at $\sqrt{s_{NN}} = 2.76$ TeV,” *Phys. Rev.*, vol. C88, p. 044910, 2013.
- [18] E. Schnedermann, J. Sollfrank, and U. W. Heinz, “Thermal phenomenology of hadrons from 200-A/GeV S+S collisions,” *Phys. Rev.*, vol. C48, pp. 2462–2475, 1993.
- [19] C. Tsallis, “Possible Generalization of Boltzmann-Gibbs Statistics,” *J. Statist. Phys.*, vol. 52, pp. 479–487, 1988.
- [20] J. Adam *et al.*, “Centrality dependence of the charged-particle multiplicity density at midrapidity in Pb-Pb collisions at $\sqrt{s_{NN}} = 5.02$ TeV,” *Phys. Rev. Lett.*, vol. 116, no. 22, p. 222302, 2016.
- [21] N. Jacazio, “Production of identified and unidentified charged hadrons in Pb-Pb collisions at $\sqrt{s_{NN}} = 5.02$ TeV,” 2017.
- [22] S. Wheaton and J. Cleymans, “THERMUS: A Thermal model package for ROOT,” *Comput. Phys.*

- 656 *Commun.*, vol. 180, pp. 84–106, 2009.
- 657 [23] B. Dönigus. Private communication.
- 658 [24] R. Scheibl and U. W. Heinz, “Coalescence and flow in ultrarelativistic heavy ion collisions,” *Phys.*
659 *Rev.*, vol. C59, pp. 1585–1602, 1999.
- 660 [25] A. Polleri, J. P. Bondorf, and I. N. Mishustin, “Effects of collective expansion on light cluster
661 spectra in relativistic heavy ion collisions,” *Phys. Lett.*, vol. B419, pp. 19–24, 1998.
- 662 [26] F. Becattini, E. Grossi, M. Bleicher, J. Steinheimer, and R. Stock, “Centrality dependence of
663 hadronization and chemical freeze-out conditions in heavy ion collisions at $\sqrt{s_{NN}} = 2.76$ TeV,”
664 *Phys. Rev.*, vol. C90, no. 5, p. 054907, 2014.
- 665 [27] F. Becattini and J. Manninen, “Centrality dependence of strangeness production in heavy-ion col-
666 lisions as a geometrical effect of core-corona superposition,” *Phys. Lett.*, vol. B673, pp. 19–23,
667 2009.